Urban Climate 49 (2023) 101513

Contents lists available at ScienceDirect

Urban Climate

journal homepage: www.elsevier.com/locate/uclim

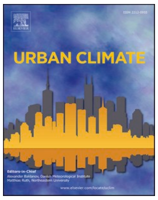

Finding common ground: A methodology for city-scale subsurface thermal modelling

M.J. Kreitmair[a,*], N. Makasis[a], A. Bidarmaghz[b], K. Menberg[c], R. Choudhary[a,d], K. Soga[e]

[a] Department of Engineering, University of Cambridge, Trumpington Street, CB2 1PZ, UK
[b] School of Civil and Environmental Engineering, University of New South Wales, Sydney, Australia
[c] Institute of Applied Geosciences, Karlsruhe Institute of Technology, Kaiserstraße 12, 76131 Karlsruhe, Germany
[d] Data-Centric Engineering, Alan Turing Institute, UK
[e] Department of Civil and Environmental Engineering, University of California, Berkeley, USA

ARTICLE INFO

Keywords:
Subsurface urban heat islands
Underground climate change
Large-scale numerical modelling
Heat transfer

ABSTRACT

The presence of anthropogenic infrastructure within the ground under cities can act to increase the temperature of the subsurface in a phenomenon known as the subsurface urban heat island effect. Large city-scale numerical subsurface temperature models accounting for both the heat fluxes stemming from human-made structures as well as hydrogeological variation are often computationally prohibitive due to the vastly different scales of modelling required. We present a novel and scalable methodology for the determination of the subsurface thermal climate beneath urban centres at a holistic scale, grouping volumes of ground into archetypes according to common thermal behaviours, identified using supervised machine learning algorithms. We apply this methodology to two boroughs in the centre of London, UK, with the results showing good agreement with a higher-resolution model for one of the boroughs. We further demonstrate the scalability of the approach by modelling the boroughs sequentially, where the second borough was modelled at little to no additional computation cost at a loss of accuracy in the local depth-averaged temperature between 0.10 and 0.23 degrees Celsius. This methodology is an important step towards determining large-scale subsurface climate beneath cities, providing insights for various applications, such as an improved understanding of geothermal energy potential.

1. Introduction

1.1. *Subsurface urban heat island effect*

The ground beneath densely populated urban centres has seen increasing use for residential and commercial spaces (e.g. basements, underground parking, etc.), transport networks (e.g. underground transit systems), industrial processes, and energy applications (e.g. ground-source heat pumps, underground district heating networks, etc.). Such structures embedded within the ground act as sources and sinks of heat, causing large-scale underground temperature anomalies, a phenomenon known as the Subsurface or Underground Urban Heat Island (SUHI/UUHI) effect (Lokoshchenko and Korneva, 2015; Bidarmaghz et al., 2019). The impact of this

---

* Corresponding author.
E-mail address: mk2040@cam.ac.uk (M.J. Kreitmair).

https://doi.org/10.1016/j.uclim.2023.101513
Received 22 December 2022; Received in revised form 22 March 2023; Accepted 23 March 2023

effect on groundwater temperatures and underground climates has been widely acknowledged (Noethen et al., 2023). Menberg et al. (2013a) investigate the impact of anthropogenic heat fluxes on subsurface temperature and its long-term evolution using a statistical analytic heat flux model, finding a significant spatial heterogeneity in the heat flux from buildings into the ground beneath the city of Karlsruhe, Germany, ranging from -100 to more than 1×10^4 mW/m^2, with the heterogeneity in part due to hydrological and surface cover variation within the study area. In a further study, comparing measured groundwater temperatures across six German cities, Menberg et al. (2013b) identify local hotspots, with temperature increases of up to 20 °C, located underneath city centers. Indeed, Previati et al. (2022) found that as much as 85% of the annual heat accumulation beneath the metropolitan area of Milan, Italy, was contributed by buildings, surface infrastructures and tunnels. Attard et al. (2016) found local temperature increases of up to 4.5 °C under the city of Lyon, France, and an annual heat flow of 4.5 GWh into the ground from underground structures, concluding that the thermal impact of these should be accounted for in geothermal potential mapping. Rotta Loria et al. (2022) illustrate the importance of accounting for the presence of and heterogeneity in infrastructure in the subsurface when determining the extent of SUHIs. Through deployment of a sensor network within the Chicago Loop district, the study measured temperatures within underground structures 25 °C higher than the undisturbed ground temperature, as well as differences of as much as 15 °C between different types of structures. The importance of varying usage of subsurface structures is also emphasised by Becker and Epting (2021), where an increase of up to 2 °C was measured between the daily temperature averages of commercial underground parking spaces within Basel, Switzerland, during times of COVID-19 lockdown periods and times of regular usage. Furthermore, the authors found that underground infrastructure can act to absorb heat from the surrounding ground, finding that a monitored freeway tunnel within the studied region exhibited temperatures below ambient ground temperatures for 52% of the year.

Increased groundwater temperatures can also affect drinking water quality, biodiversity, and the functioning of ecosystems within groundwater and those dependent on it (Müller et al., 2014; Brielmann et al., 2011; Koch et al., 2021; Becher et al., 2022). Furthermore, elevated subsurface temperatures pose risks to public health by reducing the thermal comfort experienced in underground infrastructure, such as on underground public transport, and exacerbating heat related health issues (Jacob et al., 2008). Governance and legislative frameworks of subsurface infrastructure as well as heat flux injected into the ground are an important safeguard against detrimental utilisation of the subsurface and have been the subject of recent research (Hähnlein et al., 2013; García-Gil et al., 2020; Blum et al., 2021). A commonality between these frameworks is, among others, the consideration of temperature disturbances resulting from the presence of underground structures. However, at the European level, significant differences exist between legislative frameworks as to the tolerable change in temperature caused by, for example, shallow geothermal energy utilisation, ranging from 3–11 °C (Hähnlein et al., 2013). García-Gil et al. (2020) issued a questionnaire on management policies and cycles related to shallow geothermal energy to 13 national geological survey bodies (e.g. the British Geological Survey in the UK, Geological Survey of Austria (Geologische Bundesanstalt für Österreich), etc.), and found that the identification of areas at risk of overexploitation scored highly as a management strategy to address the problem of unsustainable shallow geothermal development. Blum et al. (2021) propose a policy framework for the sustainable thermal use of shallow groundwater, where temperature limits are based on localised background temperature values rather than generalised limits. Mapping the ground temperature under cities enables identification of opportunities for better use of geothermal energy as well as enabling the understanding of areas where increased temperatures may cause ecological harm. Large-scale temperature maps of the shallow subsurface, particularly beneath urban centres, for both the current state as well as for different future ground usage scenarios, accounting for the effect of anthropogenic heat sources, can provide the necessary knowledge of the background thermal state upon which limits can be based, as well as enable the determination of problematic ground usage trends that would trigger the requirement of policy interventions.

1.2. *Modelling of the thermal state of the subsurface*

The ground being a continuum, i.e., with heat being transported through conduction and convection, heat sources in the ground, such as basements, can significantly increase ground temperatures at considerable distances over long periods of time, as shown by Ferguson and Woodbury (2004) who found ground temperatures elevated by up to 2 °C at a distance of 50 m (laterally) from a 20 °C basement structure after a simulation period of 100 years. Consequently, determining the temperature distribution under cities requires large-scale models, accounting for hydro-thermal interactions at city scale. The difficulty in this lies in the considerable computational cost afforded by models of such scale, having to include heat sources on the order of a few metres laterally, in a model that spans several kilometres. Analytical approaches, together with geo-spatial mapping tools, are often employed to overcome this computational cost in order to quantify geothermal potential (Ondreka et al., 2007; García-Gil et al., 2015; Schiel et al., 2016; Casasso and Sethi, 2016; Tissen et al., 2021; Ramos-Escudero et al., 2021; Walch et al., 2022; Miocic and Krecher, 2022). For example, Ondreka et al. (2007) use GIS-supported mapping for an area in south-western Germany based on the German technical guidelines VDI 4640 (VDI, 2001). These guidelines were also used by Miocic and Krecher (2022) to assess regional shallow geothermal potential for the German state of Baden-Württemberg, utilising an existing database of maximum heat extraction rate for this state, while also considering the heat demand of building blocks in the assessment. Similarly, García-Gil et al. (2015) incorporate groundwater flow and open-loop geothermal systems within an analytical approach combined with GIS-supported mapping to determine the geothermal potential for the Metropolitan Area of Barcelona, showing good agreement with a finite element model made for a small portion of the domain of interest. A key assumption in this approach, however, is that there is no thermal interference between heat exchangers in the ground. A study of Vienna, Austria, by Tissen et al. (2021) identified promising locations for shallow geothermal utilisation, while accounting for parameter uncertainty. Recently, Walch et al. (2022) proposed a methodology for identifying shallow geothermal potential adopting a district heating and cooling model. Assouline et al. (2019) present a machine learning-based approach to map the

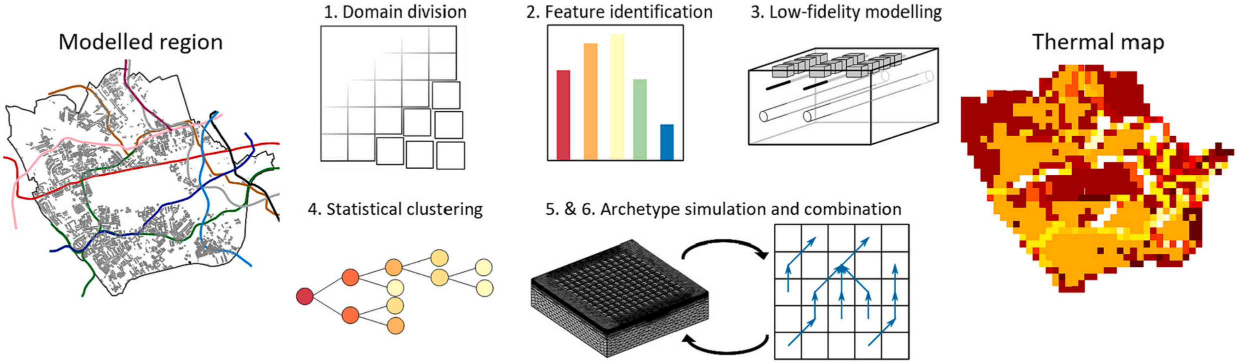

Fig. 1. Framework of proposed methodology.

geothermal potential of the very shallow (1–2 m) subsurface for the entirety of Switzerland, focusing on identifying the relevant properties of the ground.

By contrast, to avoid some of the restrictions of analytic approaches and to take account of thermal interference, large-scale numerical approaches have been implemented. For example, Bidarmaghz et al. (2020) divide the ground into horizontal planes to reduce computational cost by neglecting convection heat transport in the z-direction, resulting in a high-resolution thermal map under the Royal Borough of Kensington and Chelsea in London, UK. Large-scale evaluation of the subsurface has also been approached by a number of studies, specifically for the purposes of quantifying geothermal potential. Epting et al. (2020) combine 3D groundwater flow and heat-transport with 2D box models to assess subsurface resources for Basel, Switzerland. Barla et al. (2020) present a preliminary investigation of thermal interference between geothermal ground installations at close proximity for the city of Turin, Italy. Previati et al. (2022) introduce a city-scale 3D model for the city of Milan, where they investigate the subsurface thermal contribution of anthropogenic and natural sources, estimate the geothermal potential of a shallow aquifer, and identify that shallow geothermal systems are unlikely to significantly affect the thermal state of the subsurface and thus their utilisation should be supported. These studies, together with the global move away from fossil fuels and the drive towards the use of renewable energy sources, showcase the need to better understand heat transport within the subsurface and how to utilise it. However, the impact that anthropogenic infrastructure can have on subsurface temperatures, and thereby other aspects of the subsurface, such as groundwater ecosystem biodiversity and drinking water quality (Brielmann et al., 2011), is often not properly considered. Moreover, large-scale modelling using a single model can be restrictive due to computational costs, and increasingly difficult to undertake as the domain of interest grows in size.

1.3. *Proposed methodology*

This work proposes a novel methodology for the efficient thermal modelling of the subsurface under large urban centres, accounting for the presence of anthropogenic infrastructure in the ground and the associated heat flux, as well as hydrogeological variation, in the form of spatially varying ground water table depth and geological and hydraulic characteristics. This methodology is both scalable, in that it can be applied to modelling domains of arbitrary size, as well as extendable, i.e. once a given region has been modelled, the model may be extended to produce a thermal map of further regions at low additional computational cost, depending on the desired accuracy in temperature, with a higher accuracy requiring a greater computational expense. In this methodology, the modelling domain is divided into smaller volumes of ground in order to identify common features and thermal behaviours, in terms of temperature accumulation, across these. The identified common behaviours, in terms of heat transport processes within the subsurface, are clustered together into *archetypes*, which are then modelled at high resolution, instead of the entire domain, allowing for city-scale modelling at considerable resolution. Importantly, this methodology may be used to model subsurface temperature at large scale, given sufficient similarity in relevant features within the modeled domain, as the developed archetypes may be re-used to give outputs for a range of conditions. That is, conditions covered by the variability in the features considered within an archetype, as well as the combinations of features that lead to the same archetypal behaviour, may be represented by a single archetype. This is an important step towards holistically capturing the thermal climate underneath urban centres, taking account the impact of human-made structures in the ground, so as to better utilise the subsurface as a shallow geothermal resource.

This paper begins with an overview of the methodology in Section 2 and outlines the finite element approach used for the numerical modelling. Section 3 illustrates the proposed methodology through application to two boroughs in central London: the Royal Borough of Kensington and Chelsea (RBKC) and the City of Westminster (CoW). The results from the approach are discussed in Section 4 and are compared with high resolution results from a previous study based in RBKC. A methodology for efficient re-use of already modelled archetypes is proposed, allowing the expansion of the modelled domain at reduced computational cost. Conclusions are drawn in Section 5.

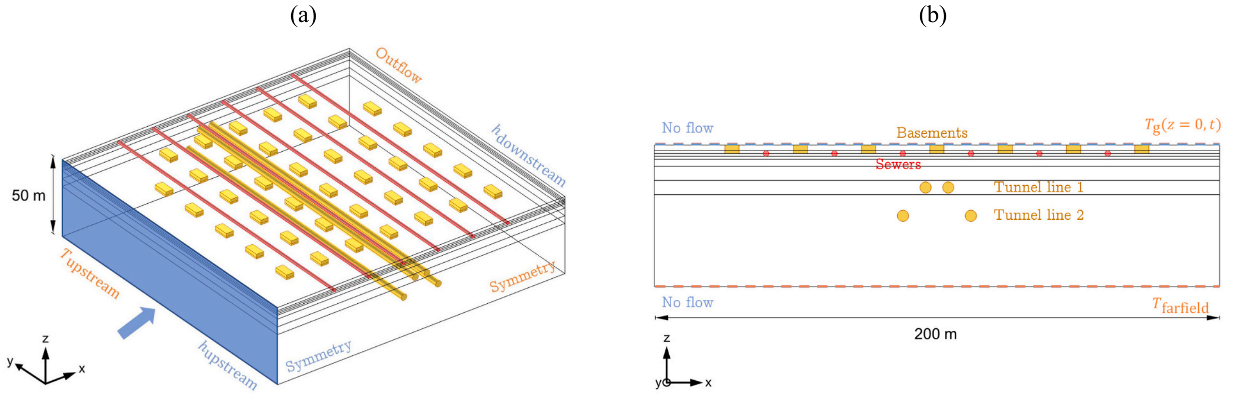

Fig. 2. Finite element model schematic showing boundary conditions for heat transfer (orange) and fluid flow (blue), and the built infrastructure elements (yellow for tunnel lines and basements and red for the sewers). The left panel shows the boundary conditions for the side surfaces and the right panel for the top and bottom surfaces.

2. Methodology

2.1. Methodology overview

The developed methodology for large-scale subsurface modelling consists of the following steps, illustrated in Fig. 1 and further detailed in following sections:

1. Division of the domain into equally-sized blocks;
2. Identification of relevant features in each block (e.g. thermal and hydrogeological parameters, presence and depth of anthropogenic heat sources, etc.);
3. Numerical simulation of blocks at low fidelity, with input values as identified, computing the volumetric temperature of blocks as output. Where groundwater flows into a block, the upstream temperature is parameterised and a range of temperatures, as would be found in the domain, is applied;
4. Statistical clustering of feature combinations according to the associated volumetric temperatures and identification of the number of archetypes based on similarity within the clusters;
5. Simulation of archetypes using high-fidelity models with input parameter values given by the average of the parameters of the models in each cluster;
6. Combination of output from high-fidelity modelling using a directed graph based on groundwater flow in the domain.

Because upstream conditions (in the form of temperature of the groundwater entering the domain) are one of the features used to determine archetypal behaviour, the final two steps require iteration between them, as will be expanded on below. Of the steps, 2–4 pertain to identifying archetypes, i.e. determining which combinations of features return thermal conditions that are suitably similar to one another to constitute a single archetype. All steps are presented in greater detail in Section 3, where the method is implemented to determine the ground temperature distribution for two boroughs in central London.

2.2. Numerical modelling

Detailed finite element modelling is used to simulate heat transfer phenomena within the subsurface blocks, with dimensions of 200 m × 200 m × 50 m, and obtain temperature distributions. The model is run at two different levels of fidelity, which are defined by the detail of the mesh and the number of elements, with the high-fidelity models containing approximately 10 times the number of mesh elements of the low-fidelity model, allowing for greater accuracy of output but requiring higher computational costs. The equations governing the physical processes in terms of conductive and convective heat transfer are given in Appendix A.

The models contain several different soil layers as well as anthropogenic structures, such as basements, sewers and tunnels, affecting the subsurface temperature distribution. An example configuration of the soil layers and such structures is shown in Fig. 2 along with lateral boundary conditions applied to the models. For all models, the thermal boundary conditions consist of the following. A prescribed temperature, T_{upstream}, at the upstream *yz*-plane, outflow at the downstream *yz*-plane, symmetry at the two *xz*-planes parallel to the groundwater flow, T_{farfield} at the bottom *xy*-plane, and varying temperature at the top *xy*-plane to account for the seasonal variation in air temperature at the surface. The latter is applied as a semi-empirical function in time and depth (Beardsmore and Cull, 2001; Baggs, 1983), fitted to local conditions, i.e.

$$T_g(z,t) = T_{0,g} - 1.07 k_v T_{\text{amp}} e^{-\epsilon z} \cos[\omega(t - t_0) + \epsilon z], \tag{1}$$

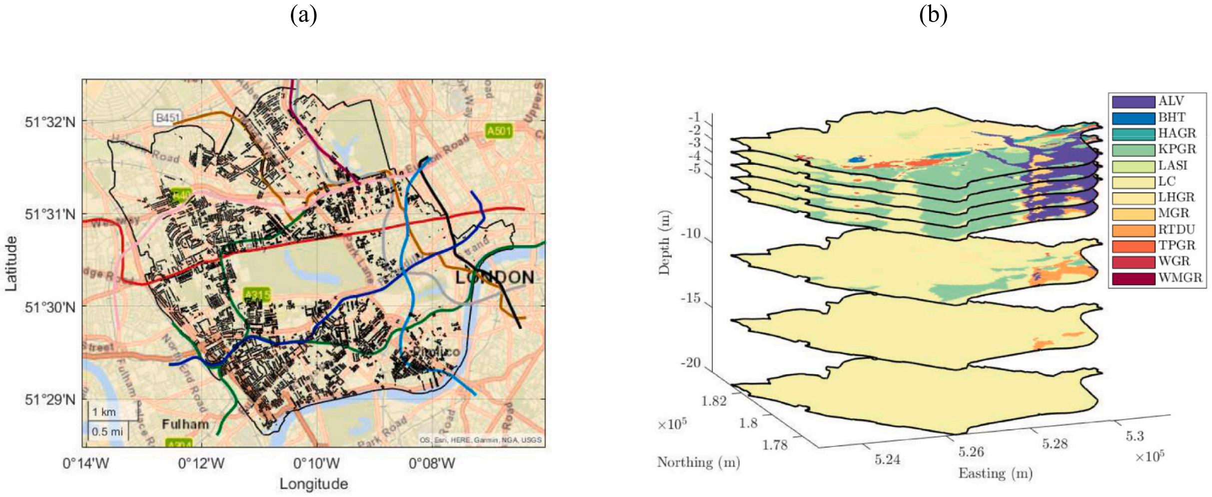

Fig. 3. Area of application: the Royal Borough of Kensington and Chelsea and the City of Westminster. Built environment within the ground, i.e. basements and train tunnels part of the London Underground Network (panel a). Geological variation within the modelled domain (panel b). Layers deeper than 20 m consist only of London Clay (LC). Details on the geologies are given in Table B.5.

Table 1
Features and ranges used for low-fidelity simulation (Price et al., 2018; Highways Agency, 2015; Santa et al., 2017; Rollin, 1987; McDonnell Cole, 2020; Low et al., 2017; Bloomer, 1981; Waterman Infrastructure & Environment Limited, 2019; Gawecka et al., 2017; Dalla Santa et al., 2020; ESSO, 2019; Roshankhah et al., 2021). Further detail on the data can be found in Appendix B.

Feature	(Range of) values	Unit
Hydrogeological conditions		
λ_{ground}	0.50–2.50	[W/(m K)]
ρ_{ground}	1.40–2.10	[Mg/m^3]
$C_{p,\text{ground}}$	0.87–1.50	[kJ/(kg K)]
$k_{h,\text{ground}}$	1.00×10^{-9} - 3.10×10^{-3}	[m/s]
$\varepsilon_{\text{ground}}$	0.35–0.50	[–]
GW_{mbgl}	2.00–18.50	[m]
Hydraulic head difference	0–13.35	[m]
Upstream groundwater temperature*	12.50–16.50	[°C]
Built infrastructure		
Tunnel depth d_{line1}	0.00–37.42	[m]
Tunnel depth d_{line2}	0.00–35.13	[m]
Basement percentage	0.0–40.18	[%]
Buildings percentage	0.0–84.48	[%]
Shade factor	0.3–1.30	[–]

*This is the only feature that is parameterised.

where $T_{0,g}$ is the mean annual ground temperature (°C), set to 12.5 °C (Price et al., 2018), T_{amp} the seasonal heating cycle amplitude (°C), found to be 8.3 °C (NCAS British Atmospheric Data Centre, 1853), $\omega = \frac{2\pi}{P}$ is the angular frequency of the heating cycle (rad) with period $P = 365$ days, $\epsilon = \sqrt{\frac{\pi}{(P\alpha)}}$, α is the thermal diffusivity of the ground (m^2/s), k_v is the shade factor coefficient (taking a value between 0.3 and 1.3 depending on the conditions present (Popiel and Wojtkowiak, 2013)), and t_0 is the day of coldest temperature after January 1st, found to be 10 days (NCAS British Atmospheric Data Centre, 1853). The initial temperature throughout the soil domains is set to T_{farfield}, while the temperatures of the basements are set to $T = 18$ °C (Bidarmaghz et al., 2020) and the sewer to $T = 15$ °C (Hawley and Fenner, 2012). For the underground train lines a time-varying temperature is applied as discussed in Section 3.2.2.

The hydraulic boundary conditions, also shown in Fig. 2 consist of prescribed hydraulic head values at the upstream and downstream *yz*-planes according to the hydraulic gradient of the block, symmetry conditions at the two *xz*-panes parallel to flow, and a no-flow condition at the top and bottom *xy*-planes (with the top plane in this case defined as the surface of the saturated soil).

3. Application of methodology

The proposed methodology is illustrated through application to two boroughs in central London, namely the Royal Borough of Kensington and Chelsea (RBKC) and the City of Westminster (CoW), shown in Fig. 3a.

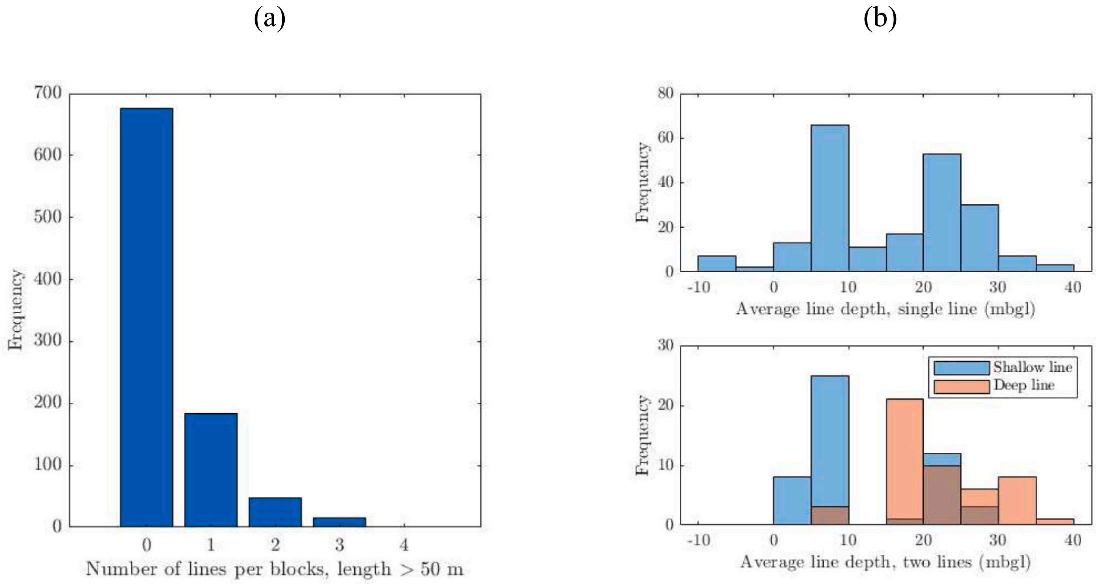

Fig. 4. Number of underground transit lines present per block in the domain (panel a) and average depth of lines in block for blocks with only one line (top of panel b) and two lines (bottom of panel b).

3.1. *Division of domain*

The domain is divided into smaller volumes of 200 m × 200 m in the *x* and *y*-directions, and 50 m in depth. This size is adopted to showcase the methodology and is the result of a compromise between computational demands and output resolution, and taking into account the resolution of available data, depth of heat sources, and extent of heat propagation. However, the block size can easily be adjusted depending on application demands.

3.2. *Identification of relevant features*

An essential step in the creation of subsurface archetypes is the identification of features that impact subsurface temperature, thereby constituting descriptors for an archetype. These features relate to both the natural and built environments and their selection is based on existing literature and understanding of subsurface heat transport processes. The importance of hydraulic and thermal conductivity values of soils on their temperatures, for example, is well established, as they relate to convection and conduction of heat, respectively. Furthermore, several studies have shown the impact of anthropogenic infrastructure on the thermal state of the ground, specifically in terms of heated basements (Tissen et al., 2021; Makasis et al., 2021) and train tunnels (Bidarmaghz et al., 2021). The features identified as impactful on ground temperature in this work are listed in Table 1, consisting of soil thermal and hydraulic properties, hydrogeological conditions, shading factor (a measure of the magnitude of thermal influence from the surface) (Popiel and Wojtkowiak, 2013), and the presence and depth of subsurface structures. The ranges presented in Table 1 cover the values identified within the domain. For the geological conditions this represents the different ground materials present as detailed in Appendix B. It is worth mentioning that data for some of these features, particularly the ground properties, may not be readily available for other cities around the world. In such cases, it is expected that using any available information to estimate these values and using lower resolution (e.g., homogeneous soil instead of multiple layers) can still provide valuable insights on the subsurface thermal processes. Moreover, some of the features, such as building footprints, can be easily obtained using software such as QGIS.

3.2.1. *Hydrogeology within domain*

The type of soil material present within a given block is crucial to the heat transport phenomena taking place, as the properties of the material determine the rate at which heat is conducted or convected. Soil properties therefore constitute key features in the identification of block archetypes. Data from the British Geological Survey (BGS), illustrated as geological layers in Fig. 3b, are used to identify the ground lithologies and distributions present in each block in the modelled domain. The hydraulic and thermal properties of the soil types present in the domain are listed in Appendix B, determined based on existing literature, including relevant studies from the area. The resolution of the geological data has informed the geometry of the block, resulting in a total of 8 layers, with changes at depths of 1 m, 2 m, 3 m, 4 m, 5 m, 7.5 m, 12.5 m, and 17.5 m. Groundwater level data are also provided by the BGS, and used to determine the hydraulic head difference in the dominant flow direction for each block and, in combination with the local hydraulic conductivity, the groundwater velocity in within a block. For the blocks with significant groundwater flow present, i.e. with a groundwater velocity of greater than 1×10^{-7} m/s, determined using the hydraulic conductivity and hydraulic head, the temperature of the water entering the domain needs to be specified. However, the upstream groundwater temperature is not known before

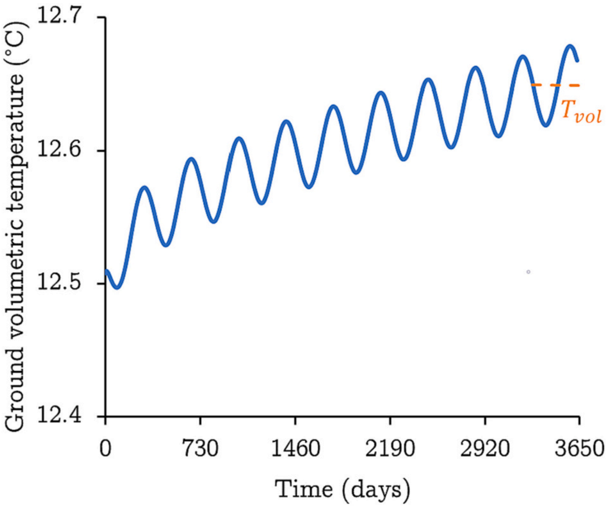

Fig. 5. Volumetric temperature distribution of the ground for a typical low-fidelity simulation.

modelling is completed. Consequently, the upstream groundwater temperature is parameterised such that for each block with groundwater flow, five possible values of upstream temperature are considered, from 12.5 °C to 16.5 °C, in 1 °C increments. These values represent a low to high influence from heat sources upstream, with 12.5 °C being the far-field temperature (Busby et al., 2011) and subsequent modelling confirming that 16.5 °C is not exceeded. A more detailed breakdown of the hydrogeology within the domain, including distributions of materials, can be found in Appendix B.

3.2.2. *Built infrastructure within domain*

Subsurface infrastructure can act as heat sources within the ground, raising the temperature and changing ambient conditions. Because this study focuses on the city of London, incorporating the underground tunnel lines is an important step, as it has been documented that some of these lines, especially those in London Clay, have accumulated significant amounts of heat in the surrounding soil, causing decline of passenger comfort during hot days (Stephen, 2016). The train lines present in the domain are shown in Fig. 3a, plotted from OpenStreetMap (OSM) data (OpenStreetMap contributors, 2017), and the distribution of the number of train lines falling within a block is shown in Fig. 4a. Three or more train lines occur in less than 2% of the blocks in the domain and therefore only up to two tunnel lines are included in the analyses, each consisting of a set of twin tunnels, 4 m in diameter. Fig. 4b shows the distribution of average line depths within a block of the domain, determined from linearly interpolating station depths (WhatDoTheyKnow, 2011) along the path of the train line, where one line is termed *shallow* and the other *deep*. Within a numerical representation of a block, tunnels are placed parallel to the *y*-axis, and centrally along the *x*-axis. The single/shallow tunnels are spaced 8 m apart, while the deep line tunnels are 24 m apart to be able to facilitate cases where the two lines are at similar depths. A temperature fluctuation based on a documented linear relationship between outside air temperature and tunnel/platform temperature is implemented (Gilbey et al., 2011). The derived platform temperatures have been fitted with a sinusoidal function $T_{\text{tunnel}} = 23 + 4\sin(2\pi t/365 - 2.044187)°\text{C}$, where time t is in days, and, for simplicity, is subsequently used as tunnel temperature boundary condition for all lines.

Further sources of significant anthropogenic heat flux in the ground are basements and sewers. Basements in the area are identified using an OSM database (OpenStreetMap contributors, 2017) and a depth of 3 m is assumed (typical for the area (RBKC, 2021)) in the numerical representation. The (right-skewed) distribution of basements, as a percentage of surface area, included in Fig. B.19 in Appendix B, shows that most blocks contain few to no basements, with a notable number around the 20% value and a sharp decline beyond that value. While varying the basement density in the modelling, each basement is assumed to have dimensions of 5 × 10 × 3 metres, and a mostly central configuration is adopted such that margins of 25 m remain between the model domain edges and basements. This geometric configuration was chosen after testing several options, including random placement of basements, and concluding that this one best captures the widest range of potential distributions. Other test configurations are not included in this work for brevity. Where more detailed information is available on the building types, these can be incorporated as an additional feature for higher resolution results, e.g., distinguishing factories from other buildings, which can have a different thermal footprint (Tissen et al., 2019). Placement of sewers is linked to the number of buildings within a block (the higher the total building area per block, the higher the number of sewers per block), as little information exists on the *in situ* location of sewers, hence requiring assumptions. The sewers are oriented along the y direction, in between rows of basements, at a depth of 3 metres below the surface. A diameter of 2 m is assumed for the sewers, estimated based on the limited available information on London's sewage network, and an average temperature of 15 °*C* (Hawley and Fenner, 2012*;* Hart and Halden, 2020*)*.

The final feature considered, though somewhat less directly related to built infrastructure, is the shade factor. This factor represents how shading affects subsurface temperature fluctuations and takes a value between 0.3 and 1.3 (Popiel and Wojtkowiak, 2013). In this work, available land cover OSM data were used to estimate the shade factor value for each block, with lower values for highly shaded

Table 2
Training features for decision tree.

Feature	Description	Unit
$\lambda_{\mathrm{ground,av}}$	Ground thermal conductivity averaged over depth	[W/(m K)]
$\rho_{\mathrm{ground,av}}$	Ground density averaged over depth	[Mg/m^3]
$C_{p,\mathrm{ground,av}}$	Ground thermal capacity averaged over depth	[kJ/(kg K)]
$k_{h,\mathrm{ground,av}}$	Ground hydraulic conductivity averaged over depth	[m/s]
$\varepsilon_{\mathrm{ground,av}}$	Ground porosity averaged over depth	[–]
GW_{mbgl}	Groundwater level - below surface	[m]
dHH	Hydraulic head difference at dominant direction	[m]
k_v	Shade factor	[–]
T_{upstream}	Upstream groundwater temperature	[°C]
$A_{\mathrm{basements}}$	Percentage of basements over surface area	[%]
$A_{\mathrm{buildings}}$	Percentage of buildings over surface area (used to determine number of sewers)	[%]
Tunnel count	Number of tunnel lines within domain	[–]
$d_{\mathrm{tunnelline1}}$	Depth of centreline of first tunnel line	[m]
$d_{\mathrm{tunnelline2}}$	Depth of centreline of second tunnel line	[m]
Tunnel In Aq	Number indicating how many tunnels are within an aquifer (in increments of 0.5)	[–]

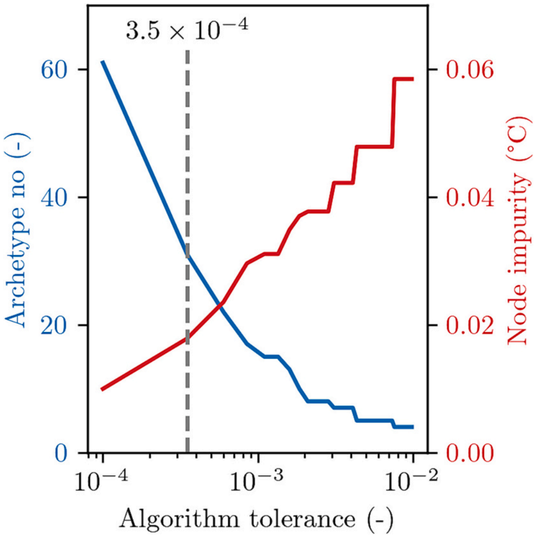

Fig. 6. Optimal tolerance to minimise the total number of archetypes generated (and thus computational costs) and node impurity, computed as MSE within a node of the decision tree and averaged over all nodes.

areas, such as woodland, and higher values for areas such as bare roads. The shade factor distribution and further information on the built infrastructure within the domain can be found in Appendix B. It should be noted that built infrastructure can change over time, when considering a period of decades. While in this work these features remain constant over time, city expansion or densification could be incorporated in the methodology, by splitting simulations in separate parts, at the expense of computational costs.

3.3. Low-fidelity simulations

Identification of the archetypes requires data on the thermal state of a block resulting from various combinations of key input features discussed above, in order for the similarity between these to be assessed. Because a large number of simulations are needed to generate the input–output relationships, low-fidelity models are used as computational speed takes priority over model output resolution at this stage. To this end, low-fidelity simulations for each block have been computed, in each case using the respective feature values from the ranges in Table 1. A total of 2086 simulations are run, one for each of the 631 blocks in the two boroughs that do not have significant groundwater flow and five for each of the 291 blocks that do and for which the upstream groundwater temperature is parameterised. Each simulation requires a few minutes to compute and extract the results. The key output of the models is the volumetric temperature of the ground within each block, from a depth of 2 metres downwards. The first 2 metres of subsurface are disregarded so as to reduce any potential noise in the data due to surface fluctuations. While this measure is not capable of presenting a detailed image of the heat transfer, the volumetric temperature is nonetheless a good representation of the thermal state of the ground and suitable for determining the thermal impact of the input features. A typical response of ground volumetric temperature over time is shown in Fig. 5. To compute a single metric to use in the archetype training stage, the average of the last (in this case, 10th) year of

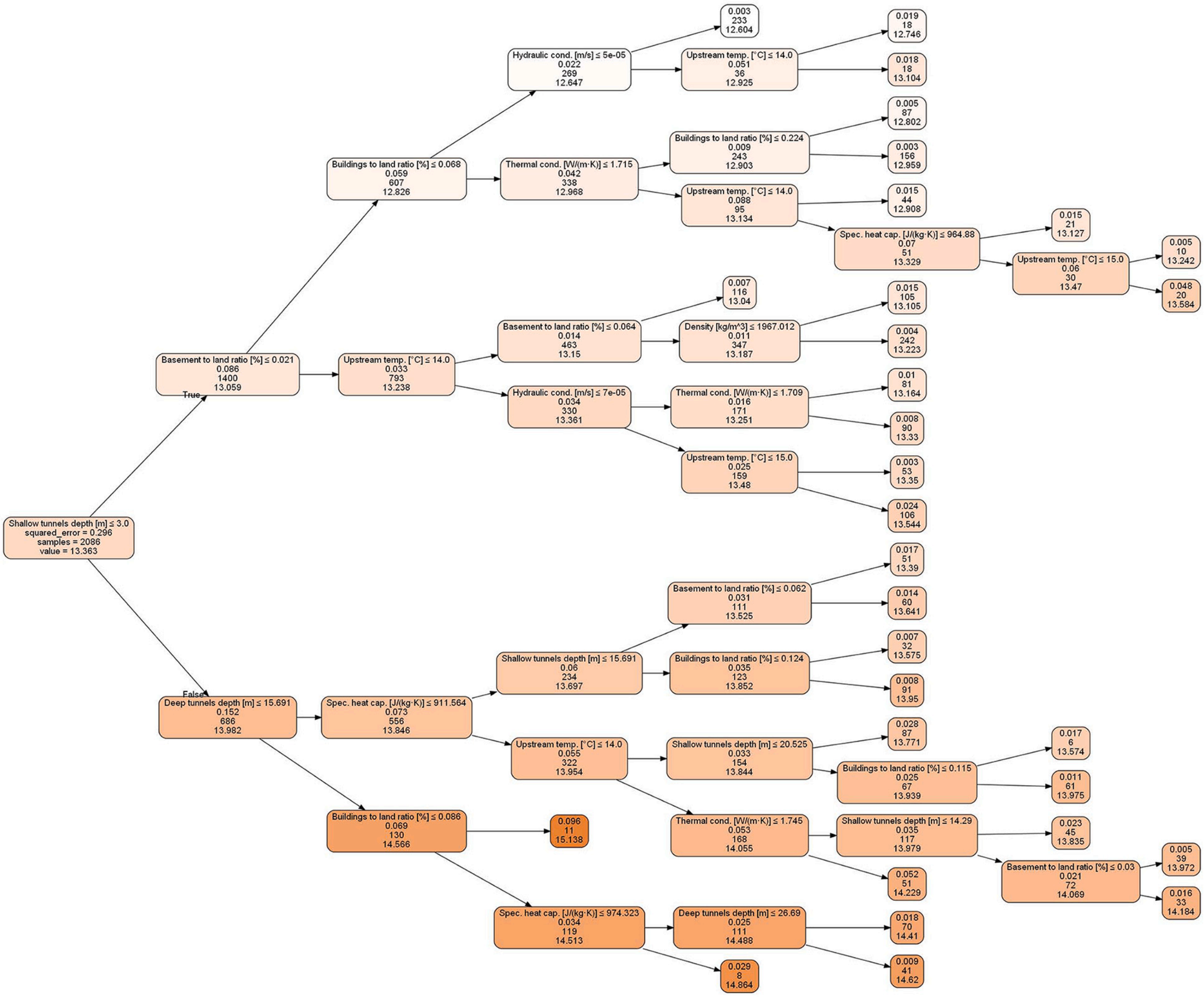

Fig. 7. Decision tree for the examined domain for the chosen tolerance of 3.5×10^{-4}. The root node (left-most) includes labels, and all nodes show the impurity (MSE), number of samples in the node out of the 2086 data points used to train it, and the mean value of the used metric T_{vol}.

simulation is computed, T_{vol} - also indicated on the figure, to ensure that thermal accumulation effects over time are accounted for. It is worth noting that different simulation durations and appropriate metrics have been investigated, to ensure the applicability of the chosen values. While 10 years have been used herein, to limit computational time costs, another suitable approach can be running each low-fidelity simulation until a thermal equilibrium has been reached.

3.4. *Identification of archetypes*

Having run the low-fidelity simulation batch and having computed T_{vol} for each feature combination, archetypes are then identified through clustering together feature combinations that produce similar output, i.e. volumetric temperature values. To this end, a regression-based decision tree is trained using the low-fidelity data, i.e. the relevant features outlined in Section 3.2 as well as further features, such as *Tunnel Count*, that provide additional information to the algorithm, shown in Table 2, and the corresponding T_{vol}. Decision trees divide the data from an initial node, or set, according to the feature that minimises the impurity, or discrepancy, of a quantity of interest within a node, in this case T_{vol}. This discrepancy may be evaluated in different ways. The most common, and the one used in this analysis, being by using the mean squared error (MSE). At each branching point, a node is chosen to be split along a feature value such that the impurity metric (i.e. the MSE) for all nodes combined (the global impurity) is minimised. More details on decision tree formulation and splitting can be found in (Breiman et al., 1984; Hastie et al., 2009). In the approach used herein, the data are split repeatedly, using different features at each branch point, until an appropriately low global impurity is reached, equal to a desired set tolerance, resulting in a collection of node branches, or a *tree*, where the leaf nodes, i.e. nodes without any further outgoing connections, designate archetypes. By setting different values for the desired tolerance, the size of the tree, and thus the number of archetypes, can be altered, with a lower tolerance requiring greater similarity within a node, hence resulting in more archetypes.

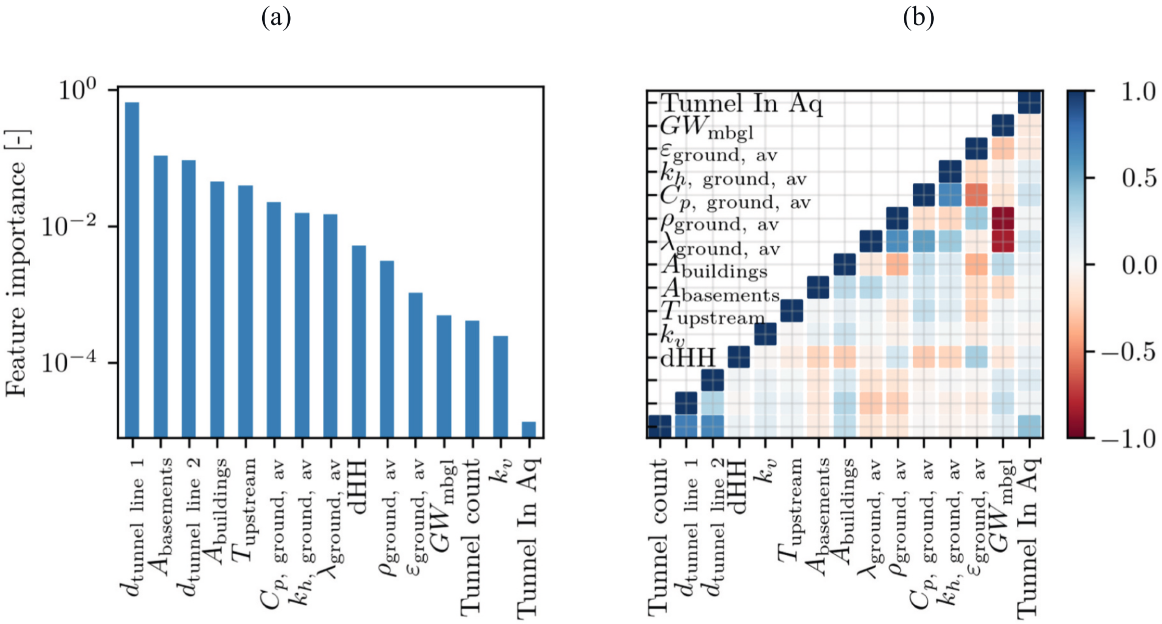

Fig. 8. Feature importance rankings (panel a), showing which features are most influential on the creation of archetypes using the decision tree, and correlation coefficient for each pair of features (b), noting that the correlation matrix is symmetrical and the *y*-axis is the same as the *x*-axis with left to right being bottom to top. The abbreviations used are introduced in Table 2.

Through adjustment of the tolerance, a balance is struck between generality of the nodes and a number of archetypes that is feasible (and practical) to simulate through high-fidelity models. That is, not having so many archetypes that the number of high-fidelity simulations becomes computationally infeasible, nor so few that distinct behaviours are merged and archetypes suffer a loss of accuracy. Fig. 6 shows how the change in the value of the recession tolerance (*x*-axis) affects node impurity (mean over all leaf nodes) (right *y*-axis) as well as the associated number of archetypes (left *y*-axis). A value of 3.5×10^{-4} is selected, resulting in a total of 31 archetypes that fit the data ranges that were used for the low-fidelity simulation and a mean impurity of under 0.02 °C, noting that the T_{vol} values from the low-fidelity simulations ranged from 12.537 °C to 15.610 °C.

The regression tree resulting from this fine-tuning is shown in Fig. 7, where the root node is on the left and each branch node gives the feature and value used for the branching, the impurity (i.e. squared error) of the volumetric temperature of the models within that node, the number of samples (of the 2086 low-fidelity combinations) contained within the node, and the average value of T_{vol}. Leaf nodes, i.e. the resulting archetypes, only show the final three of these as they are not further split. Using the tree, each block can be associated with an archetype, which can represent the thermal behaviour of the block, by starting from the root of the tree and following the branches until a leaf node is reached.

The algorithm determines which feature is most suitable to use to split a node into two others. Therefore, the features are assigned a different score according to their *importance*, with a higher score indicating that the feature play a greater role in defining the archetypes. These scores can be seen in Fig. 8a, showing that a key identifying factor for the archetypes are the presence of heat sources, especially the presence of tunnel lines. The significance of convection is also highlighted, as both the hydraulic conductivity and the temperature of groundwater entering the domain rank relatively highly. The thermal conductivity and specific heat capacity, relating to heat conduction, are also shown to play a role on determining the archetypes. On the other hand, the remaining ground properties as well as the shade factor are shown to have little influence over the archetypes of the examined domain, for the chosen tolerance. The *Tunnels in Aquifer* metric was the least influential, due to the fact that most tunnels in this domain are within the clay and therefore most values for this parameter are (close to) 0. However, it is expected that in other regions with different ground/tunnel conditions its importance can be high. It is important to acknowledge that, given the nature of the data, there can be correlations between the features and these correlations are shown in Fig. 8b. Some correlations can be seen between the different ground properties, which is expected since these properties all relate to certain materials. Strong correlation is also observed between the groundwater level and the ground thermal properties, since the depth and amount of saturated soil can affect these values.

3.5. High-fidelity simulations & production of temperature map

The final steps of the methodology are the simulation of the identified archetypes at high fidelity and the combination of their outputs, i.e. the area-averaged temperatures at specific depths, into a large-scale thermal map. The high-fidelity simulations consist of a comparatively larger number of mesh elements (about 10 times), allowing for higher resolution of outputs, but requiring higher

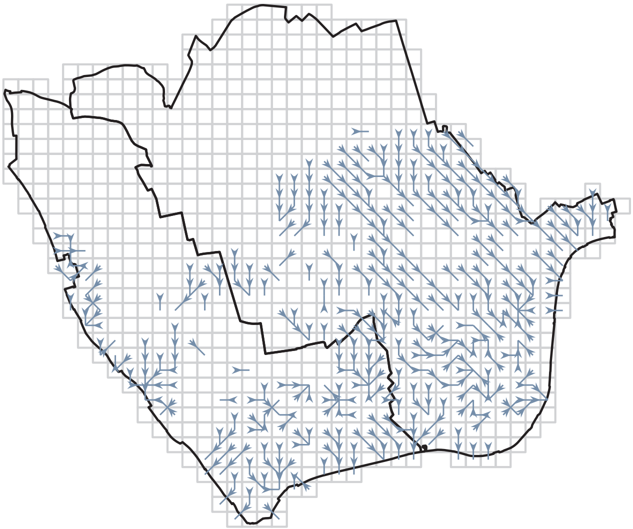

Fig. 9. Connected graph of the groundwater flow in the modelled region, indicating direction of influence of upstream groundwater temperatures and defining boundary conditions for downstream blocks.

computational cost, in this case on the order of several hours. Because one of the features used to identify archetypes is the temperature of the groundwater flowing into a block, T_{upstream}, which is unknown prior to high-fidelity model simulations and therefore parameterised during the low-fidelity simulation step (see Section 3.2.1), some of the archetypes generated may not be allocated to blocks within the modelled domain and hence do not require high-fidelity simulation.

To identify which archetypes need to be simulated, a groundwater connectivity directed graph is created, determined from data on the groundwater level, hydraulic gradient, and the hydraulic conductivity within the domain, shown in Fig. 9. Two blocks are considered to be connected by groundwater flow if the groundwater velocity, calculated using $v_{\text{GW}} = \frac{k_{h,\text{ground}}}{(d\text{HH}/L_{\text{block}})}$, exceeds a threshold of 1×10^{-7} m/s (equivalent to less than 1 cm per day). This graph informs which blocks have significant groundwater flow into them and thus the order in which blocks are associated with archetypes, to ensure that when a block passes through the tree its T_{upstream} value is known. Blocks that do not have flow into them, i.e. do not have an arrow connecting into them, are examined first and the corresponding archetypes are simulated at high fidelity. The temperature of the groundwater exiting their domain is computed as one of the outputs of the simulation, which then serves as T_{upstream} input for blocks they connect to in the graph. For blocks with multiple sources of groundwater flow, the T_{upstream} values are averaged. Following this process, all nodes in the domain are iteratively associated with an archetype and, where needed, new high-fidelity simulations are computed until all nodes belong to an archetype and all required archetypes have been simulated. Finally, from the solved archetype simulations the desired outputs can be computed, such as (but not limited to) area-averaged temperatures at different depths to create temperature maps of the subsurface.

4. Results and discussion

4.1. Results and archetype differences

A complete list of the archetypes for the investigated domain, the Royal Borough of Kensington and Chelsea (RBKC) and the City of Westminster, in London, is provided in Table 3, giving the average feature values for the blocks assigned to each archetype. Since the values of the features for each archetype are defined as an average over all the blocks that are characterised by the archetype, there can be cases where discrete features take a non-integer value. This can happen because, for that archetype, these discrete features are not key in the branching of the path from the root of the tree to the leaf for the specific archetype. In these cases the discrete features values are rounded to the nearest integer. For example, for Archetype 16 the average value of *Tunnel Count* is taken to be 1.00 instead of the computed 1.10 and a single train line is modelled in the high-fidelity model corresponding to this archetype. The degree of influence of the features defining each archetype varies, as shown in Section 3.4 and Fig. 8a. To showcase some of the more influential archetype features, such as the presence of tunnels in the subsurface, it is worth exploring some archetype feature breakdowns in more detail.

The presence of anthropogenic influences is shown to be the strongest predictor of ground temperature. Particularly regarding tunnel lines, it is apparent from Table 3 (and perhaps intuitive) that ground temperature tends to be higher, the more tunnel lines are present in the domain. Similarly, a greater presence of basements and sewers (the latter being indicated by a higher value of *Area building percentage*) are associated with higher temperatures with other factors being held the same. For example, comparing archetypes 0 and 9, both of which have no tunnels and very similar upstream temperatures but the latter has a 28% coverage of buildings, with the associated greater number of sewage pipes extending through the block, increasing the volumetric temperature by 0.44 °C. Furthermore, the temperature of the groundwater entering the block also acts as a source of heat, highlighted in comparing archetypes

Table 3
List of the 24 archetypes found in domain.

Archetype No.	Tunnel count	Tunnel 1 depth [m]	Tunnel 2 depth [m]	Hydraulic head difference, dHH [m]	Shade coeff. k_v, [–]	Upstream GW temperature, T_{upstream} [°C]	Area basement percentage [%]	Area building percentage [%]	Avg. thermal conductivity λ [W/(m · K)]	Avg. density ρ [kg/m^3]	Avg. specific heat capacity, C_p [J/(kg·K)]	Avg. hydraulic conductivity k_h [m/s]	Avg. porosity ε [–]	GW level [mbgl]	No. of tunnels in aquifer [–]	Volumetric temperature [°C]
0	0.00	–	–	3.34	0.59	13.07	0.07	1.23	1.64	1970.16	886.33	8.21×10^{-8}	0.49	3.35	0.00	12.60
1	0.00	–	–	2.63	0.55	13.50	0.15	1.33	1.69	1963.38	932.35	1.07×10^{-4}	0.49	3.08	0.00	12.75
3	0.00	–	–	2.95	0.76	12.74	0.22	15.91	1.66	1977.03	883.78	2.05×10^{-8}	0.50	2.75	0.00	12.80
5	0.00	–	–	2.66	0.74	13.76	0.18	26.91	1.75	1971.14	964.17	4.81×10^{-5}	0.49	2.01	0.00	12.91
4	0.00	–	–	2.50	0.74	12.85	0.42	39.37	1.63	1965.81	884.88	4.31×10^{-8}	0.49	4.07	0.00	12.96
9	0.00	–	–	2.43	0.73	13.05	4.28	28.26	1.69	1969.27	913.14	4.26×10^{-7}	0.49	3.09	0.00	13.04
2	0.00	–	–	4.02	0.42	14.50	0.04	1.58	1.73	1974.87	938.96	5.91×10^{-5}	0.49	2.01	0.00	13.10
10	0.00	–	–	1.34	0.71	13.34	15.99	36.73	1.73	1952.60	961.05	1.41×10^{-5}	0.48	3.67	0.00	13.10
12	0.00	–	–	2.64	0.78	14.50	13.72	39.73	1.64	1961.31	912.00	1.37×10^{-5}	0.48	4.12	0.00	13.16
11	0.00	–	–	2.63	0.74	13.07	17.47	32.64	1.70	1978.60	902.49	4.93×10^{-7}	0.49	2.06	0.00	13.22
7	0.00	–	–	2.57	0.72	14.50	0.14	30.45	1.77	1962.60	989.85	9.61×10^{-5}	0.49	2.01	0.00	13.24
13	0.00	–	–	1.52	0.76	14.50	15.22	37.05	1.73	1975.00	939.09	2.04×10^{-5}	0.48	2.02	0.00	13.33
14	0.00	–	–	1.04	0.76	14.50	15.37	35.53	1.78	1966.10	975.77	1.09×10^{-4}	0.48	2.00	0.00	13.35
16	1.10	7.31	0.88	3.47	0.89	12.82	1.96	23.55	1.67	1981.70	876.11	5.71×10^{-8}	0.50	2.20	0.03	13.39
21	1.00	26.75	–	4.52	0.63	13.50	0.00	2.32	1.76	1973.93	950.05	2.01×10^{-5}	0.48	2.00	0.00	13.57
18	1.00	23.27	–	2.54	0.62	14.00	0.61	3.10	1.68	1976.71	903.03	3.96×10^{-6}	0.49	2.23	0.00	13.58
17	1.25	8.06	1.80	2.49	0.77	12.83	16.65	34.13	1.65	1975.43	879.02	1.79×10^{-7}	0.50	2.92	0.03	13.64
20	1.14	9.72	1.07	2.36	0.72	13.55	10.12	37.42	1.75	1967.62	961.84	4.57×10^{-5}	0.48	2.04	0.72	13.77
23	1.20	6.74	1.83	2.98	0.67	14.50	6.72	40.11	1.73	1967.59	948.25	3.23×10^{-5}	0.49	2.07	0.80	13.83
19	1.00	24.68	–	2.30	0.77	12.97	6.25	43.70	1.60	1955.07	889.39	1.26×10^{-6}	0.49	5.18	0.00	13.95
22	1.00	25.08	–	2.22	0.80	13.80	6.41	50.87	1.63	1951.99	936.07	1.51×10^{-5}	0.48	4.76	0.00	13.97
25	1.00	23.13	–	1.94	0.75	14.50	15.54	48.10	1.67	1954.81	952.41	2.66×10^{-5}	0.48	3.44	0.00	14.18
26	1.06	13.01	0.35	1.78	0.74	14.50	10.78	35.91	1.77	1969.64	965.02	7.80×10^{-5}	0.48	2.00	0.59	14.23
28	2.00	11.09	20.29	2.00	0.76	13.17	5.93	37.70	1.66	1961.00	905.77	3.50×10^{-7}	0.49	4.30	0.17	14.41
29	2.00	20.60	30.79	1.63	0.76	13.58	4.41	51.24	1.57	1941.66	896.84	1.65×10^{-5}	0.49	6.68	0.08	14.62
30	2.00	7.18	24.25	1.96	0.85	13.00	5.59	29.25	1.77	1957.83	992.02	7.87×10^{-5}	0.48	2.00	0.75	14.86
27	2.00	6.58	20.32	6.72	0.83	13.83	0.50	3.51	1.73	1965.57	961.64	4.90×10^{-5}	0.49	2.00	1.00	15.14

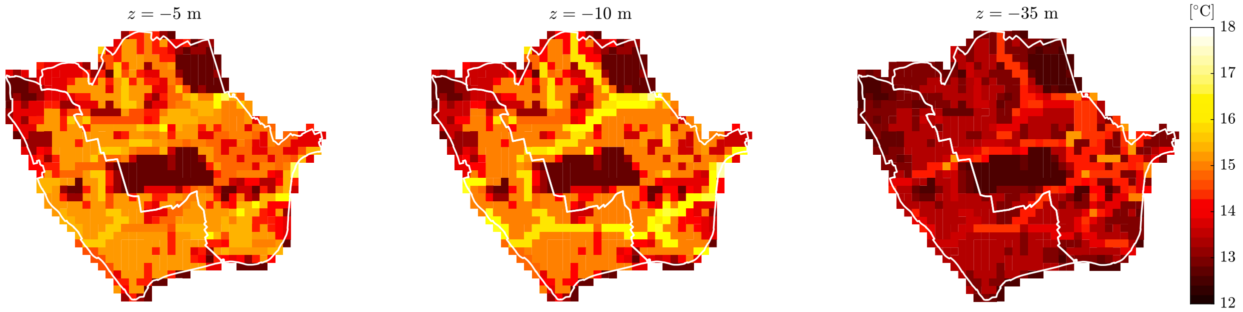

Fig. 10. Output of the archetypes-based methodology: area-averaged temperature distribution averaged over the last year of simulation, shown at 10 m, 20 m, and 35 m below ground level.

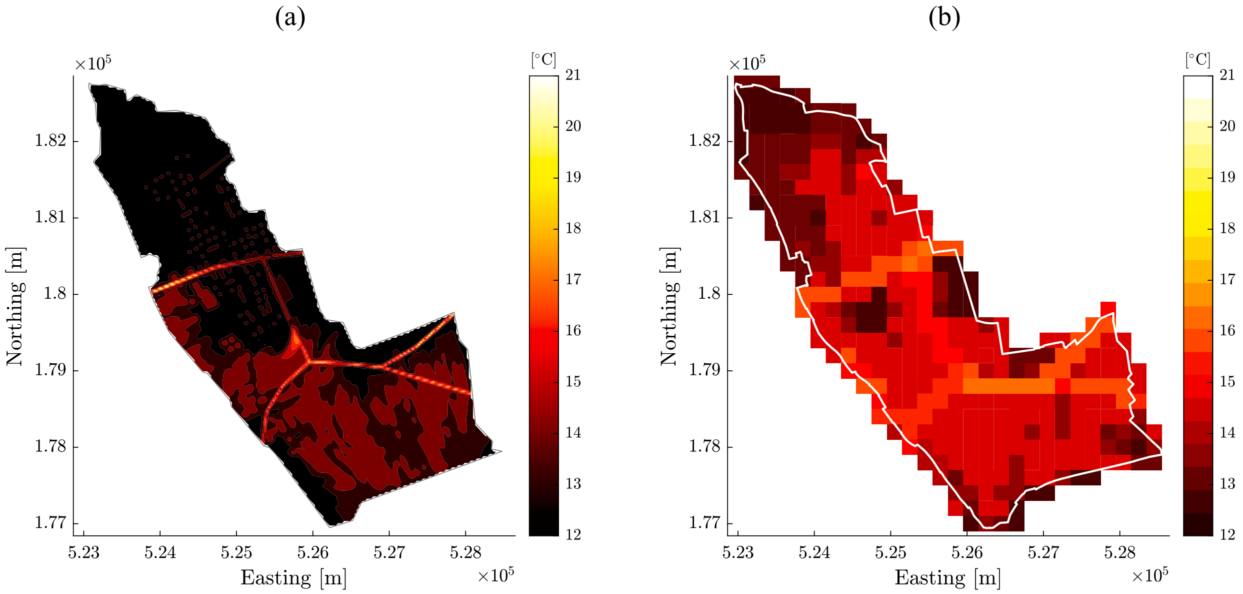

Fig. 11. Comparison of thermal map produced from a high resolution model (panel a) and archetypes-based model output (b) at a depth of 20 m below ground level, averaged over the 25th year of simulation.

27 with 30. The former exhibits a volumetric temperature of that is 0.27 °C higher than that of 30, despite the latter having a 26 % greater building ratio. The impact of this increase on volumetric temperature is (more than) counteracted by the upstream groundwater temperature, which is 0.83 °C less, giving rise to the discrepancy in T_{vol} that is observed between the two archetypes.

Another important feature is the groundwater flow velocity, which is given by a combination of hydraulic head difference and the hydraulic conductivity within a block. Generally speaking, faster groundwater flow will act to distribute heat from heat sources and 'flush' them further downstream out of the block, thereby preventing accumulation of heat and reducing the volumetric temperature. This effect is illustrated in the comparison between archetypes 19 and 22 which exhibit almost identical volumetric temperatures, despite a difference in the upstream temperature of 0.83 °C. This is due to a factor of magnitude difference in the average hydraulic conductivity in the blocks, resulting in a similar difference in the groundwater flow velocities in the permeable layers (given the similarity in the hydraulic head difference). Hence, the groundwater entering the block at a (relatively higher) temperature of 13.80 °C for archetype 22, is carried through the block quicker than for archetype 19, resulting in less accumulation and thereby roughly the same T_{vol}. Importantly, the comparison of these two archetypes shows that the nature of the decision tree algorithm, where branches are created and each node is split into two sequentially, enables the creation of archetypes that have similar volumetric temperatures, but different thermal processes (since the paths from the root node of the tree to the archetype leaf for archetypes 19 and 22 are significantly different).

A good understanding of the archetypes and the features that comprise and differentiate them can provide confidence in their combined use to obtain large-scale information. Importantly, the above methodology can be used to provide detailed temperature distributions within the domain. Results from this work, namely area-averaged temperature outputs at different depths of the domain, are presented in Fig. 10, where temperature distributions are shown for 10, 20 and 35 m below ground level under the modelled domain, as an example. In these subsurface temperature maps, the underground tunnel lines are clearly visible, as regions of higher temperatures crossing the area. Moreover, the presence of Hyde Park, being devoid of heated infrastructure, can be seen as an area of relatively cool ground in the centre of the domain. Residential areas with heated basements, such as the west of the domain, also show increased temperatures compared to, for example, Hyde Park. These observations provide confidence in the results.

4.2. *Comparison to high resolution model*

The accuracy of the proposed methodology in generating subsurface temperatures is examined through comparison of the archetype-based ground temperatures against those from a high-resolution model developed by Bidarmaghz et al. (2020). In this model of RBKC, the domain is divided vertically into a series of thermally coupled planes within which conduction and convection are modelled. Heat sources, specifically basements and underground tunnel lines, are abstracted for computational tractability and certain ground properties are homogenised. The temperature at a depth of 20 metres below ground level, averaged over the last year of the 25-year simulation, is shown in Fig. 11a. The presence of the underground train tunnels is clearly visible as lines of elevated temperature, i.e. the Central Line running almost horizontally across the northern part of the domain, and the Circle, District, and Piccadilly Lines crossing and branching in the southern part. Additionally, the southern regions of the domain exhibit areas of higher temperature (approximately 14.5 °C) due to the heat convected by groundwater flow from the basements present just below the surface.

For comparison, a thermal map generated using the archetypes-based method for the same region and year is shown in Fig. 11b. The area-averaged temperatures in the 200 m × 200 m blocks show good agreement with the results from the high resolution model, with the effect of underground train tunnels captured as blocks with higher area-averaged temperatures, and with over 50% of the blocks being within 0.6 °C of the block-averaged temperatures obtained from the high-resolution results. The distribution of basements is also reproduced in the archetypes results, showing an area of lower temperature where basements are absent at the north end of the borough, as is the case in the high resolution results. The apparently higher temperature in the northern part of the domain is likely due to the inclusion of sewer networks in the arechetypes-based methodology, which are implemented in blocks containing buildings, even in the absence of basements (see Section 3.2.2), a heat source that is not incorporated in the high resolution modelling.

It is apparent that the results of the archetype methodology are of lower resolution and capture less of the spatial variability, reflecting the chosen grid-size. However, the key features of the domain are represented well. It is worth noting that this grid-size, and thereby the resolution of the archetypes-based results, can be varied based on the region modelled and the resolution of the data available. While modelling an entire domain within one model can provide more detailed results, the results from the proposed methodology are at a resolution that is useful for a range of applications such as large-scale geothermal resource assessment and large-scale future scenario forecasting. Moreover, this methodology allows for full 3D element modelling and reduces potential scaling issues, present when a numerical model has large differences in scale of its modelled features. It is also significantly less computationally restrictive without the requirement for large computers, and can be a scalable approach which reduces in computational requirements as more and more domains are modelled, data is gathered, and archetypes are created.

4.3. *Extendability of the methodology*

4.3.1. *Overview & extendability options*

The proposed methodology regards large-scale thermal mapping, for which the regions to be mapped can be incorporated in stages, due to data availability, administrative reasons, or project timelines among others reasons. Therefore, while having the entire dataset to begin with can lead to a more complete outcome, with a single large decision tree, it is important to assess how extension of an already mapped region can be achieved. To assess this aspect of the methodology, in Section 4.3 the two boroughs modelled in this work, RBKC and CoW, are examined in sequence, instead of computing the thermal map for the combined RBKC and CoW region as done in the previous sections, identifying and comparing ways to thermally map CoW, given that the thermal map of RBKC is completed.

No tree approach. The first and lowest cost option is to use the decision tree created for the already mapped region, i.e. RBKC, as well as the respective archetype outputs. The block data for the new domain, CoW, are passed through the decision tree for RBKC and each block is associated with an archetype which has already been simulated, the outputs of which can then be used to populate the thermal map for CoW. While no additional numerical modelling is required for high-fidelity simulations of the archetypes, this approach relies on features that determine the thermal state of the ground, i.e. hydro-geology and built infrastructure features, having similar value ranges across the two regions. That is, the archetypes for RBKC must also be representative for the blocks in CoW. This can be a valid assumption in certain cases, especially when the dataset of the already mapped region is large enough. However, if discrepancies occur in the features present within the two regions, then this approach to the domain extension runs the risk of reducing computational cost and time at the expense of accuracy.

Fully modelled approach. The second option comes at the greatest computational cost, and entails generating a new separate regression tree for CoW only and running an additional set of high-fidelity models for the identified archetypes in the new region. As part of this option, the datasets for RBKC and CoW are treated individually, with the exception of values for T_{upstream} from blocks at the border of the two regions, i.e. for blocks in CoW that have groundwater flow coming from blocks in RBKC the T_{upstream} is known after RBKC is thermally mapped. Whilst being the most computationally expensive, this approach contains the least inaccuracies, as the archetypes result from a decision tree trained with data from the relevant region. For this approach, the decision trees of both regions, when mapped separately, can be found in Appendix C.

Table 4
Training features and weighting, representing the expected magnitude of impact of a given feature on archetype analysis output.

Feature	Weight
$\lambda_{\text{ground,av}}$	0.50
$\rho_{\text{ground,av}}$	0.25
$C_{p,\text{ground,av}}$	0.15
$k_{h,\text{ground,av}}$	0.25
$\varepsilon_{\text{ground,av}}$	0.10
GW_{mbgl}	0.10
dHH	0.50
k_v	0.15
T_{upstream}	0.60
$A_{\text{basements}}$	0.50
$A_{\text{buildings}}$	0.50
Tunnel Count	0.20
$d_{\text{tunnelline1}}$	0.75
$d_{\text{tunnelline2}}$	0.25
Tunnel In Aq	0.20
Archetype T_{vol} (from lo-fi data)	1.00

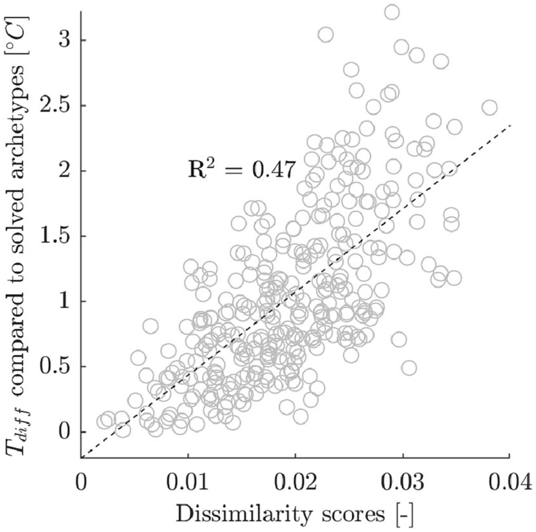

Fig. 12. Dissimilarity score against average temperature difference between each pair of archetypes from the two boroughs investigated in this work.

Dissimilarity approach. The third and final option presented is a compromise between the previous two. After the decision tree for the new region (CoW) is created, the determined archetypes (for CoW) are compared to those of the already modelled region (RBKC), and the pairs that are sufficiently similar are identified, for which the already computed archetypes are used for both regions removing the need to simulate the new ones. The remaining archetypes for CoW are simulated as in option two, meaning that overall fewer high-fidelity simulations are needed for this option compared to the fully modelled approach - but more than in option 1 (for which no additional archetypes need to be simulated). Due to the steps involved in this option, it is presented in detail in Section 4.3.2. The choice of option for extension depends on several factors, particularly the similarity of the feature combinations within the new domain to those of the already generated one, the computational resources available, and the size of the additional domain among others.

4.3.2. *Extendability: dissimilarity approach*

In cases where some regions have been computed and mapped and nearby regions are selected for subsequent mapping (and the features of the two regions are somewhat similar), information from the computed regions can be used to reduce the computational costs of modelling the subsequent region. This reduction relates to the last part of the methodology, where high-fidelity models are

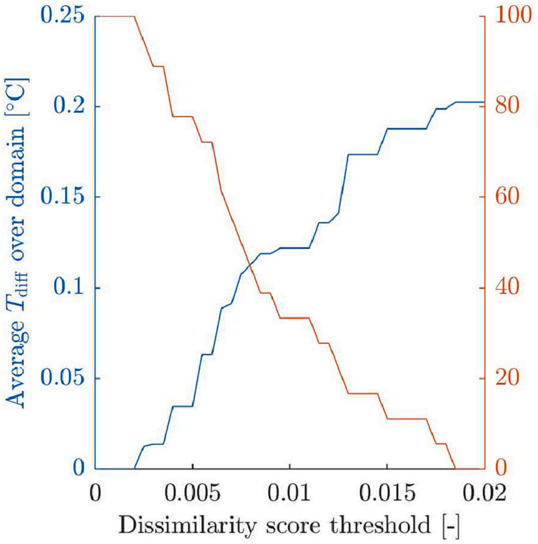

Fig. 13. Average T_{diff}, computed for each block in CoW, and the percentage of archetypes that need computing (representing computational savings), for different values of dissimilarity score threshold (below which archetypes from CoW are not solved but the equivalent similar archetype output from RBKC is used).

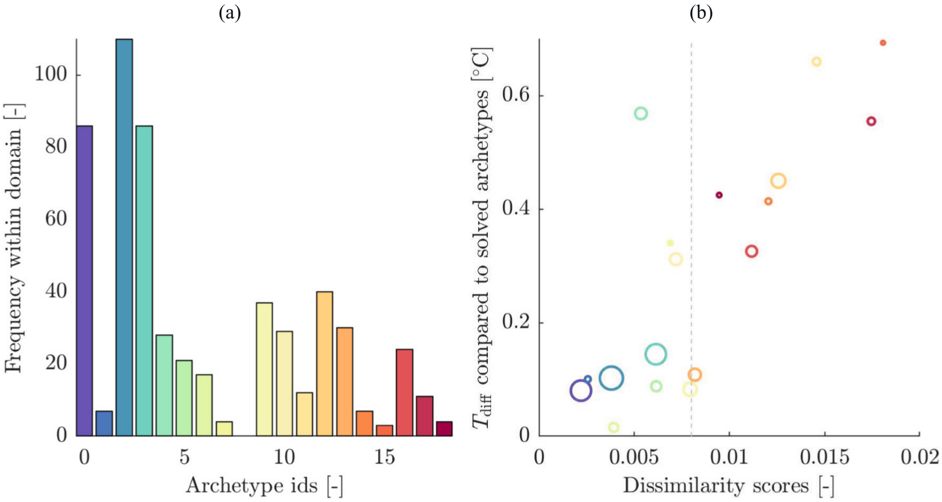

Fig. 14. Frequency of (number of blocks associated with) computed archetypes for the expanded region of CoW (panel a), and a scatter plot of the T_{diff} between computing an archetype from CoW and using a similar one from RBKC, including only the most similar archetype from RBKC for each archetype of CoW (b). The colours of the archetypes correspond to the archetype id and the size of the markers to the frequency of blocks for each archetype. The dashed gray line represents a dissimilarity score threshold of 0.008.

created, after the archetype features have been identified. By examining the features of the archetypes from both computed and non-computed regions, archetypes of sufficient similarity can be identified such that simulation outputs from the already computed archetypes can be used instead of requiring new computations. The measure of similarity is done using a *dissimilarity score*, computed as the Mean Absolute Error for all weighted features, after normalisation, where a low score suggests high similarity between two archetypes. The weights used represent each feature's impact on the archetype output and are determined based on engineering judgement, as illustrated in Table 4, noting that different values could be used depending on the scenario. A good understanding of the physical processes is essential in determining these values, as the outputs can be sensitive to the weights, particularly the order of importance for features, and inconsistencies can lead to incorrect characterisation of archetypes. Further work is expected to streamline this process.

RBKC and CoW are considered separately and new separate regression trees are created for each of them (see Appendix C),

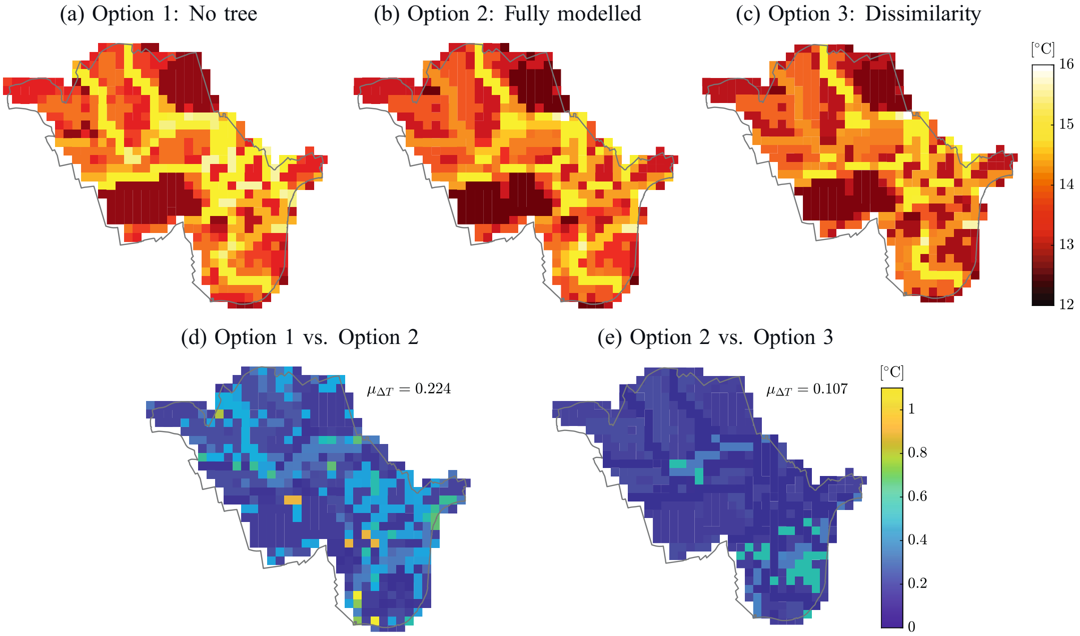

Fig. 15. Extendability results: Panels (a), (b), and (c) show the (depth-averaged) heat map produced for CoW when following extendability options 1, 2, and 3, respectively. The temperatures shown are for the last year of simulations, in this case 50th year. Panels (d) and (e) show the temperature difference for each block in CoW between the different approaches, assuming that option 2 is the most reliable one, since it generates archetypes using the specific data from the area.

identifying the archetypes in each borough. The archetypes for both boroughs are simulated, for the purpose of this analysis, enabling the calculation of not only the dissimilarity score between two archetypes from different boroughs, but also the difference in the temperature output, T_{diff}. Here, T_{diff} is defined as the mean absolute error in the computed depth-averaged temperature over the last year of simulation. Fig. 12 shows the plot of T_{diff}, calculated for every possible pairing of the 18 archetypes identified in RBKC and the 18 archetypes identified in CoW, against the dissimilarity score determined for the same pair. The scatter shows that there exists some correlation between the two quantities, with a higher variance in T_{diff} at higher values of dissimilarity score. Importantly, at low values of dissimilarity score, the variance of T_{diff} is small and the values are relatively low, suggesting that a low value for dissimilarity could indicate suitably similar archetypes in terms of their output.

To identify a suitable dissimilarity score threshold, i.e. one below which archetypes for CoW are sufficiently similar so as not to require computation but rather the output from the most similar archetype from RBKC, the average T_{diff} over the entire domain (computed for each block within the domain and averaged) as well as the computational costs (in terms of the percentage of archetypes from CoW that need to be computed) are plotted for different values of a dissimilarity score threshold. This is shown in Fig. 13, indicating that a threshold of 0.008 results in an average T_{diff} of about 0.11 and would require less than half (44%) of the created archetypes for CoW to be computed. Fig. 14 further examines this scenario, showing that the archetypes that have the lowest dissimilarity score are also the ones representing the greatest number of blocks in the region. Therefore, the archetypes that require computing (i.e. those with a dissimilarity score higher than the threshold) are ones that only have a few blocks associated with them, which is reasonable as they comprise more rare cases with potentially multiple elements affecting the thermal state of the ground.

4.3.3. Comparison of extendability options

The three extendability options introduced above are now examined in their applicability for the region of CoW, after having thermally mapped RBKC. Depth-averaged temperature results for each option are illustrated in Fig. 15(a–c), showing similar patterns, with the areas close to tunnel lines being hotter and a colder area in the South West, which is Hyde Park. However, discrepancies between them are apparent, illustrated in plots (d) and (e), comparing Option 1 and 3, respectively, with Option 2, which is considered the most accurate since it computes archetypes specific to CoW. As expected, Option 1 shows the greatest discrepancy (compared to Option 2), with a mean depth-averaged temperature difference of 0.224 °C and maximum differences for a handful of blocks of around 1 °C. Option 3 shows a lower difference to Option 2, with a mean depth-averaged temperature difference of 0.107 °C and maximum differences of around only 0.6 °C (as can also be seen in Fig. 14b). For a practical interpretation of these results, a study on the city of Cardiff showed that an inaccurate estimation of the subsurface volumetric temperature between 0.9 and 1.1 °C can result in an error in the shallow geothermal potential estimation between 8.5 and 11% (Makasis et al., 2021).

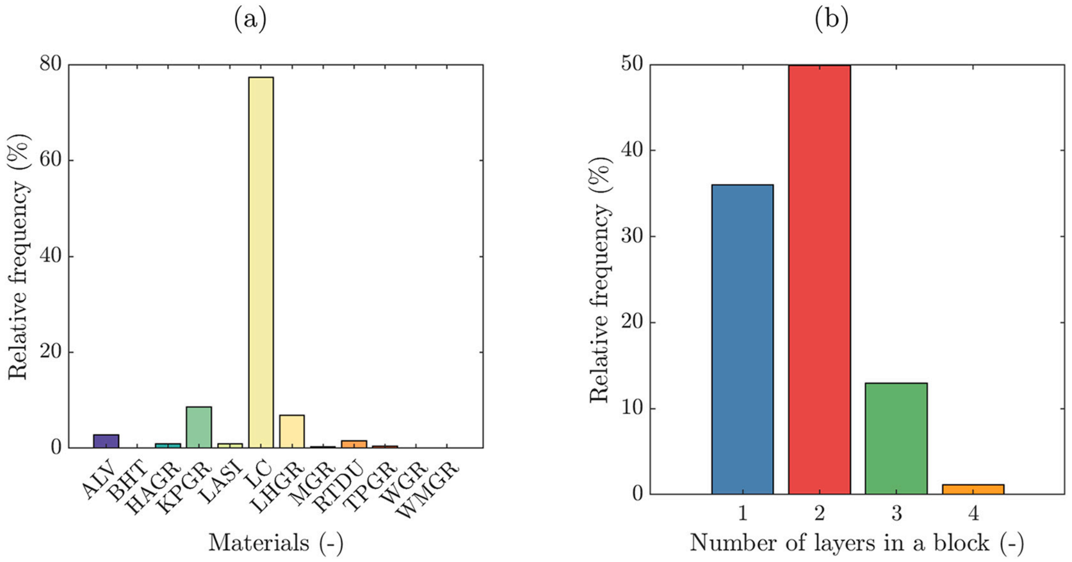

Fig. B.16. Soil types within the area of application in terms of the material volume (panel a) and number of unique layers/soil types per block (b).

Table B.5
Thermal and hydraulic properties of geological materials present in the modelled domain and concrete material used for heat sources (Price et al., 2018; Highways Agency, 2015; Santa et al., 2017; Rollin, 1987; McDonnell Cole, 2020; Low et al., 2017; Bloomer, 1981; Waterman Infrastructure & Environment Limited, 2019; Gawecka et al., 2017; Dalla Santa et al., 2020; ESSO, 2019; Roshankhah et al., 2021). Thermal diffusivity was calculated according to $\alpha = \frac{\lambda}{(\rho C_p)}$. Where appropriate, top values in a row represent partially saturated conditions and bottom values fully saturated conditions.

Geology/Material	Average depth range [m]	Thermal conductivity, λ [W/(m K)]	Density, ρ [Mg/m^3]	Specific heat capacity, C_p [kJ/(kg K)]	Effective porosity, ε [–]	Hydraulic conductivity, k_h [m/s]	Thermal diffusivity, α [m^2/s]
Alluvium, ALV	0.32–3.50	0.91	1.40	1.40	0.50	1.09×10^{-3}	4.64×10^{-7}
		1.70	1.70	1.50			6.67×10^{-7}
Boyn Hill Gravel, BHT	0.05–3.00	0.77	1.60	1.10	0.35	7.65×10^{-5}	4.38×10^{-7}
		2.50	1.90	1.44			9.14×10^{-7}
Hackney Gravel, HAGR	0.32–3.66	0.77	1.60	1.10	0.35	3.10×10^{-3}	4.38×10^{-7}
		2.50	1.90	1.40			9.14×10^{-7}
Kempton Park Gravel, KPGR	0.72–5.47	0.77	1.60	1.10	0.35	5.66×10^{-4}	4.38×10^{-7}
		2.50	1.90	1.44			9.14×10^{-7}
Langley Silt, LASI	0.15–2.00	1.00	1.81	1.00	0.5	1.00×10^{-9}	5.52×10^{-7}
		1.70	2.10	1.20			6.75×10^{-7}
London Clay, LC	5.47–50.00	1.00	1.60	0.87	0.50	1.00×10^{-9}	7.18×10^{-7}
		1.70	2.00	0.87			9.77×10^{-7}
Lynch Hill Gravel, LHGR	0.19–5.26	0.50	1.60	1.10	0.35	7.51×10^{-5}	2.84×10^{-7}
		2.40	1.90	1.44			8.77×10^{-7}
Made Ground, MGR	0.03–2.45	1.40	1.61	1.20	0.35	2.10×10^{-7}	7.25×10^{-7}
		2.20	2.10	1.20			8.73×10^{-6}
River Terrace deposits, RTDU	7.05–8.05	0.50	1.70	0.70	0.50	2.03×10^{-4}	4.20×10^{-7}
		2.50	2.10	1.30			9.16×10^{-7}
Taplow Gravel, TPGR	0.23–1.55	0.77	1.60	1.10	0.35	3.26×10^{-4}	4.38×10^{-7}
		2.50	1.90	1.44			9.14×10^{-7}
Worked Ground, WGR	0.01–0.60	1.40	1.61	1.20	0.35	2.10×10^{-7}	7.25×10^{-7}
		2.20	2.10	1.20			8.73×10^{-7}
Infilled Ground, WMGR	0.00–0.70	1.40	1.61	1.20	0.35	2.10×10^{-7}	7.25×10^{-7}
		2.20	2.10	1.20			8.73×10^{-7}

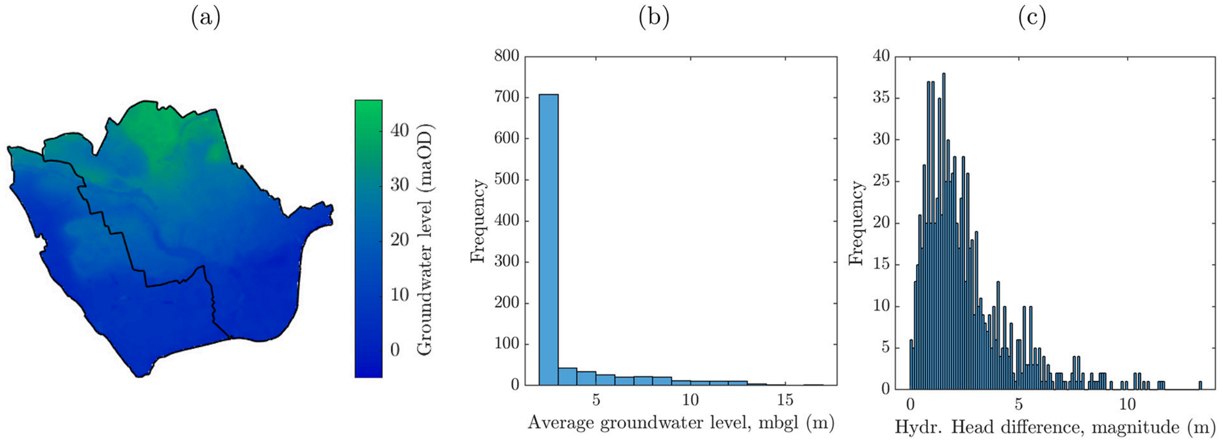

Fig. B.17. Hydrology in the area of application showing the groundwater level with respect to the Ordinance Datum (panel a), and histograms of the groundwater level with respect to the surface level (c), and of the magnitude of the hydraulic head difference (c) for all blocks.

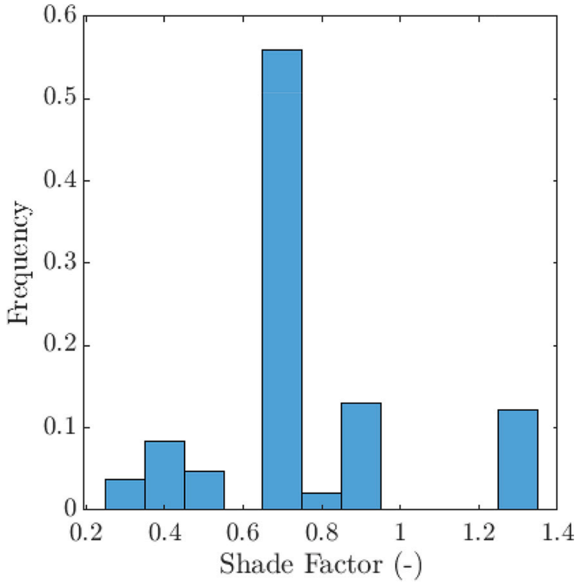

Fig. B.18. Histogram of shade factor values within domain.

In contrast to accuracy, Option 1 is the most favourable approach in terms of computational requirements. This option required a computational time of a few minutes and can be undertaken on any average personal computer. Option 2 necessitated generation of 18 archetypes, each requiring about 3 h to run on a computer with two 2.10 GHz processors (Intel(R) Xeon(R) Silver 4116 CPU, 12 cores), for a total of about 54 h of computation. Option 3 only required the computation of 8 of the generated archetypes for CoW, resulting in a total of 24 h of computation. In this case, any of these options could be considered suitable, depending on the application, project timelines and resources available, noting that these values scale with a larger area and therefore the savings can be more significant, depending on the scenario. If accuracy is needed and Option 1 is not suitable as the chosen method, it can still be a good first approximation, given its very low computational cost. Option 2 is the safest approach, while Option 3 requires engineering judgement and understanding of the problem context, in this case being able to reduce the computational time by over 50% but resulting in some small differences in the output.

4.4. Limitations and future work

The presented methodology can be used to create subsurface thermal maps of large regions. While there is potential for diminishing

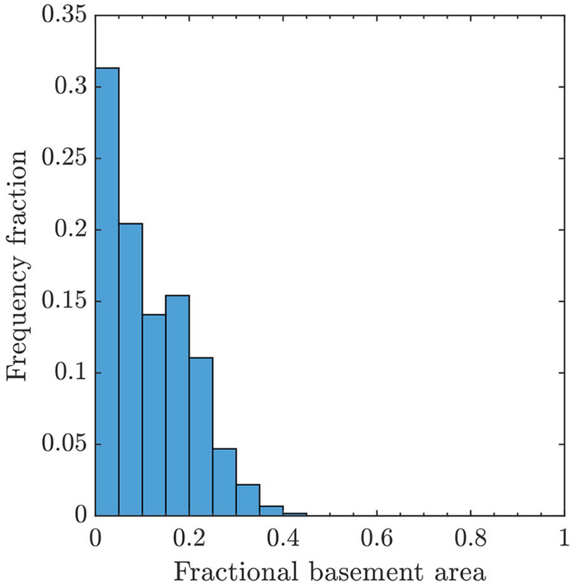

Fig. B.19. Histogram of the basement to block area fraction values within domain. Only non-zero values are included, due to a large number of blocks having no basements.

computational costs as the database of existing simulated archetypes increases, the computational cost to produce a thermal map for a region is still significant. A substantial portion of those computational requirements, with regards to time, is due to obtaining the data required to build the decision tree, done in step 3 via low-fidelity simulations of the blocks in the area. These simulations required a few minutes in this work, however a large amount of blocks needed simulating (over 2000), which could be a potential barrier to the use of the methodology. One potential solution to this problem could be the use of machine learning approaches to create a numerical emulator for the low-fidelity FE model, able to predict the output of interest, in this case T_{vol}, in a matter of seconds instead of minutes. This would significantly reduce the necessary time for step 3 of the methodology and would enable the creation of the decision tree without requiring numerical simulations. The creation of this emulator, however, requires a large dataset for it to be trained on, since the training data need to cover a wide range of feature inputs to be representative. While outside the scope of the presented work introducing the methodology, using emulators instead of numerical modelling for step 3 of the methodology is expected to be investigated in future work.

The other significant computational cost comes in step 5, where the archetypes are simulated in high fidelity. For this step, computational savings could be obtained by mapping a smaller region first and then extending the map, using some of the knowledge obtained for the first region, as showcased in Section 4.3.

Finally, potential improvements of this methodology could be achieved by introducing more output variables in the regression decision tree creation. This would mean using more variables than the T_{vol} to split the tree nodes, such as, for example, annual thermal accumulation, which could capture the thermal processes in more detail. While feasible, this approach introduces additional complexities, e.g. identifying the weight each of the outputs should have on the splitting of a node, and therefore is also expected to be investigated in future work.

5. Conclusion

This work proposes a flexible, scalable, extendable, and efficient methodology for large-scale subsurface modelling. In this methodology the entire domain is split into smaller, computationally manageable blocks of chosen dimensions - depending on the requirements of the application, which are used to identify common thermal patterns within the domain. This is done by modelling blocks at low fidelity, using numerical modelling with a relatively coarse mesh but sufficient to capture the main thermal processes taking place and creating regression trees with the generated output. The creation of the regression tree produces the feature combinations (i.e. the values for the natural and anthropogenic characteristics) that result in distinct subsurface thermal behaviour, or *archetypes*. These archetypes can therefore be used to represent a large number of subsurface blocks and determining the main archetypes within a large domain means that the entirety of that domain can be modelled by only a few small-scale models, enabling modelling at high fidelity and resolution. Importantly, the groundwater conditions and the continuity between the blocks is incorporated in the methodology, by parameterising the temperature of the groundwater entering the blocks and following an iterative approach to combining the final results. The methodology is not restricted by the size of the domain to be modelled, unlike current numerical modelling approaches, and can be used in stages, producing a thermal map of a region and then extending to more regions when required. Moreover, the framework encourages a large collaborative approach to modelling the subsurface, where simulated archetypes can be stored in a database and used by others when identifying locations with similar archetype features, reducing computational requirements with an increasing database (and use of the methodology).

The proposed methodology is applied to two boroughs in central London, the Royal Borough of Kensington and Chelsea and the City of Westminster, for which access to subsurface data, such as hydro-geological conditions, is made available through collaboration with the British Geological Survey. The application results in 27 unique archetypes, utilising the volumetric temperature as the metric of interest. Differences in the volumetric temperature of up to 2.5 °C are found between the archetypes, which is significant considering the size of the blocks, suggesting that significantly different subsurface thermal states exist within these boroughs. Since the thermal state of the subsurface can impact areas such as groundwater ecosystems, biodiversity, drinking water quality, and shallow geothermal energy applications, this methodology can lead to better monitored, safer subsurface conditions, as well as better-informed designs and better performance for shallow geothermal systems. The analysis identified that the main features distinguishing subsurface thermal processes (and thus comprising the archetypes) were the anthropogenic influences, such as the presence of train tunnels and basements, as well as the hydrogeological conditions, noting that train tunnels in the deeper layers of the model (consisting of London Clay) resulted in the archetypes with the hottest subsurface. The temperature results of one of the boroughs (RBKC) are compared to those of a single large-scale subsurface model of the area, exhibiting reasonable agreement.

A key feature of the methodology is its extendability, i.e. the option to extend the modelled domain, and the resulting subsurface heat map, from an already modelled region. For this purpose, three approaches are presented, with different degrees of computational cost traded off against accuracy. Testing of these approaches by extension of the thermal map from the borough of Kensington and Chelsea to the City of Westminster indicated that the approach utilising a dissimilarity metric for comparing the blocks in the extension domain to those in the domain already modelled offers a good option to extend the modelling cheaply and with reasonable accuracy. Further possible avenues for improving the methodology and making it more accessible have been briefly discussed and will be investigated in detail in future work.

CRediT authorship contribution statement

M.J. Kreitmair: Conceptualization, Methodology, Validation, Formal-analysis, Investigation, Visualization, Writing-original-draft. **N. Makasis:** Conceptualization, Methodology, Software, Formal-analysis, Investigation, Visualization, Writing-original-draft. **A. Bidarmaghz:** Methodology, Writing-review-editing. **K. Menberg:** Methodology, Writing-review-editing. **R. Choudhary:** Conceptualization, Writing-review-editing, Supervision, Funding-acquisition. **K. Soga:** Supervision, Funding-acquisition.

Declaration of Competing Interest

The authors declare that they have no known competing financial interests or personal relationships that could have appeared to influence the work reported in this paper.

Data availability

The data that has been used is confidential.

Acknowledgements

This work was supported by CMMI-EPSRC: Modeling and Monitoring of Urban Underground Climate Change (EP/T019425/1), by the Centre for Smart Infrastructure & Construction (EP/N021614/1) and the Centre for Digital Build Britain at University of Cambridge, as well as AI for Science and Government (ASG), UKRI's Strategic Priorities Fund awarded to the Alan Turing Institute, UK (EP/T001569/1). The financial support for Kathrin Menberg via the Margarete von Wrangell program of the Ministry of Science, Research and the Arts (MWK) of the State of Baden-Württemberg is gratefully acknowledged.

Appendix A. Numerical modelling: governing equations

Physical processes are incorporated using the conductive and convective heat transfer equation and Darcy's law, i.e.,

$$(\rho C_p)_{\text{eff}}\frac{\partial T_g}{\partial t}+\rho_f C_{p,f}\mathbf{v}_f\cdot\nabla T_g+\nabla\cdot\left(-\lambda_{\text{eff}}\nabla T_g\right)=0, \tag{A.1}$$

$$\mathbf{v}_f=-\frac{K}{\mu_f}\left(\nabla p_f-\rho_f\mathbf{g}\right), \tag{A.2}$$

$$\nabla \cdot \rho_f \left[-\frac{K}{\mu_f} \left(\nabla p_f - \rho_f \mathbf{g} \right) \right] = 0. \tag{A.3}$$

where ρ_{eff} is the effective density (kg/m^3), $C_{p,\mathrm{eff}}$ the effective specific heat capacity (J/(kg K)), t is time (s), ρ_f is the fluid (groundwater) density (kg/m^3), C_{pf} is the specific heat capacity of the fluid (J/(kg K)), $\mathbf{v_f}$ is the Darcy velocity of the fluid (m/s), λ_{eff} is the effective thermal conductivity (W/(m K)), the permeability K (m^2) of the material is related to the hydraulic conductivity k_h (m/s) by $\frac{K}{\mu_f} = \frac{k_h}{(\rho_f \mathbf{g})}$, μ is the dynamic viscosity of water (Pa · s), and p_f is the pressure of water (Pa).

Appendix B. Data engineering for low-fidelity analysis: soil types within domain, geological variations, shade factor, basement distribution

This section presents details on the data used for the low-fidelity analysis and the distributions found within the domain. The type of soil present within a block is crucial to the heat transport phenomena, as the material properties determine how well heat is conducted or convected. Soil properties therefore constitute key features for identifying the block archetypes. Fig. B.16a shows the volumetric density distribution across soil types within the domain and Fig. B.16b the number of unique layers that exist within a block. London clay (LC) is the most common soil material, present throughout the domain below a depth of 20 m. In fact, just over 35% of all blocks within the domain consist solely of LC. About 50% of the blocks contain two soil types, most of which are either Kempton Park gravels (KPGR) or Lynch Hill gravels (LHGR), both overlaying LC. Less than 15% of the blocks contain three different soil types, the majority of which consist of a first layer of either Alluvium (ALV) or Langley Silt, overlaying gravel (KPGR or LHGR) and LC. Finally, only about 1% of the blocks consist of 4 separate soil types. The soil types and materials within the modelled domain and the assumed thermal and hydraulic properties for each are presented in Table B.5. These values were obtained from literature including publications and technical reports, however, it is worth noting that reasonable assumptions were made where little information was available, such as assuming that the different types of gravel layers will have similar thermal properties. It is also worth noting that to determine the thermal and hydraulic properties of the ground for the different layers in each block, the values are averaged along the horizontal directions for a 200 × 200 m block from the original data which was on a 50 × 50 m grid (Jones and Hulbert, 2017) - noting that the hydraulic conductivity was averaged using a logarithmic mean (Jang et al., 2011).

The groundwater distribution within the domain is shown in Fig. B.17. The groundwater is naturally shallow along the river (i.e. the south eastern boundary of the domain), as well as to the western side of the boroughs, while levels are higher at the north-eastern side, driving groundwater flow mostly in a southern direction. Within individual blocks, the combination of groundwater level and elevation (averaged within each 200 × 200 m block) results in the majority of the blocks being saturated, with the groundwater level sitting at roughly 2 m below the surface. To determine the hydraulic gradients that are to be applied across block edges, the hydraulic head distribution is computed within each block, calculating the dominant flow direction and the average hydraulic head difference between block edges. The results shown in Fig. B.17c are in the form of a histogram showing the frequency of the hydraulic head difference within a block across the modelled domain.

The shade factor data are presented in Fig. B.18, in the form of a histogram showing the most frequent values within the two boroughs used in this work. The distribution of the fraction of basements to the area of each block, representing the density of basements, is shown in Fig. B.19.

Appendix C. Extendability: regression trees for separate regions

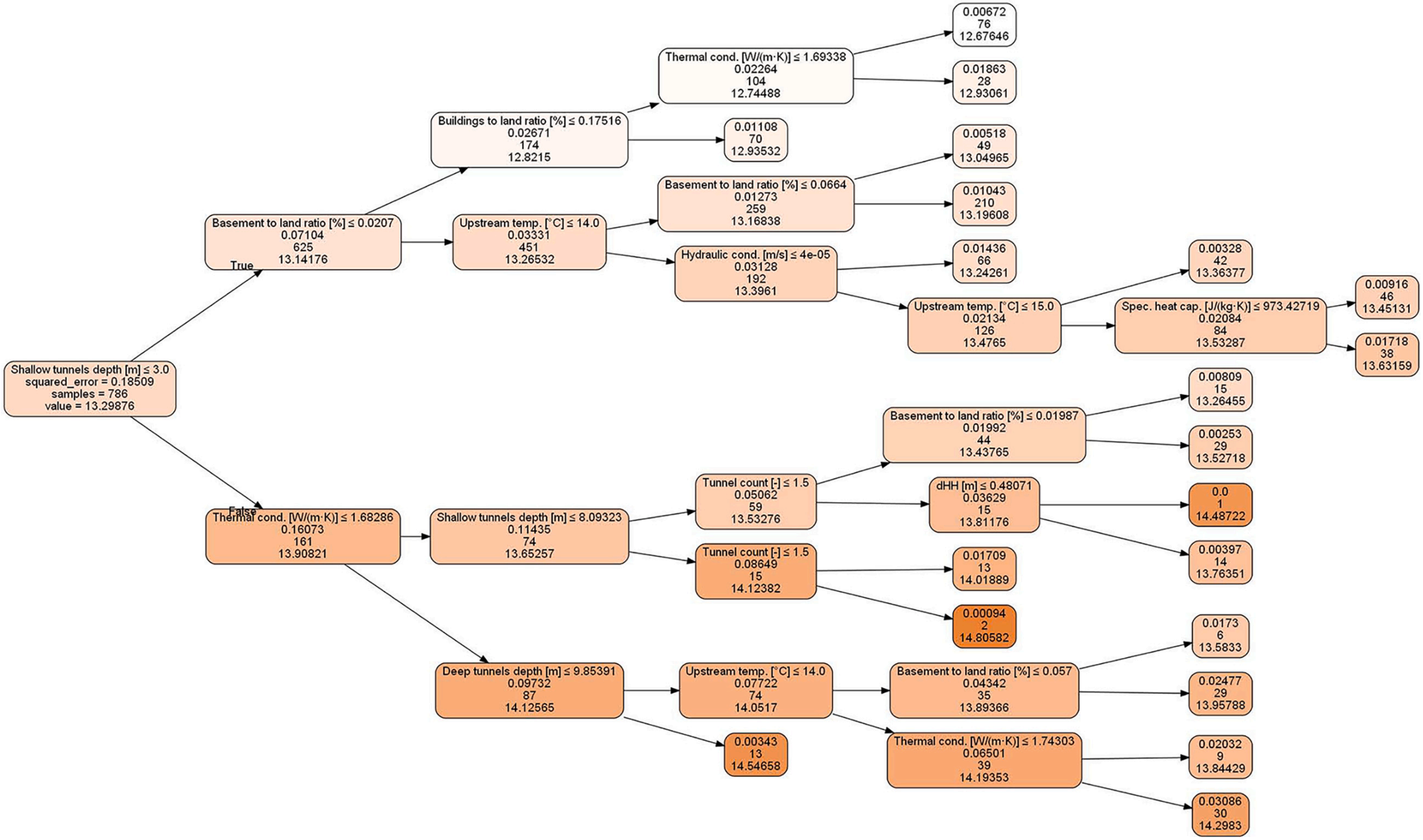

Fig. C.20. Decision tree for the RBKC domain for a chosen tolerance of 6.0×10^{-4}. The root node (left-most) includes labels, and all nodes show the impurity (MSE), number of samples in the node out of the 786 data points used to train it, and the mean value of the used metric T_{vol}.

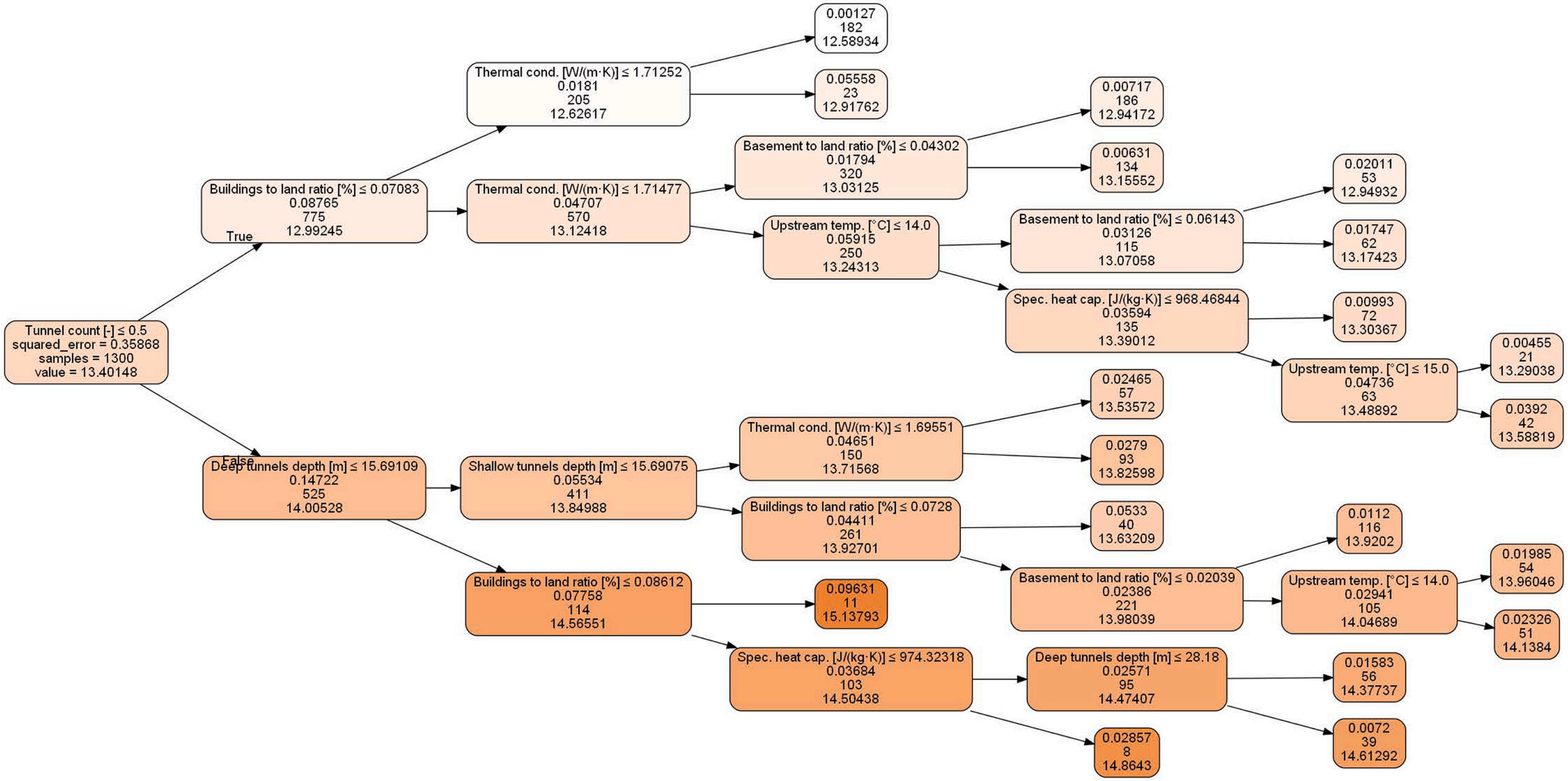

Fig. C.21. Decision tree for the CoW domain with a chosen tolerance of 6.0×10^{-4}. The root node (left-most) includes labels, and all nodes show the impurity (MSE), number of samples in the node out of the 1300 data points used to train it, and the mean value of the used metric T_{vol}.

References

Assouline, D., Mohajeri, N., Gudmundsson, A., Scartezzini, J.L., 2019. A machine learning approach for mapping the very shallow theoretical geothermal potential. Geotherm. Energy 7.

Attard, G., Rossier, Y., Winiarski, T., Eisenlohr, L., 2016. Deterministic modeling of the impact of underground structures on urban groundwater temperature. Sci. Total Environ. 572, 986–994.

Baggs, S.A., 1983. Remote prediction of ground temperature in Australian soils and mapping its distribution. Sol. Energy 30, 351–366.

Barla, M., Di Donna, A., Baralis, M., 2020. City-scale analysis of subsoil thermal conditions due to geothermal exploitation. Environ. Geotech. 7, 306–316.

Beardsmore, G.R., Cull, J.P., 2001. Heat Generation. Crustal Heat Flow, Cambridge University Press, in, pp. 23–44.

Becher, J., Englisch, C., Griebler, C., Bayer, P., 2022. Groundwater fauna downtown – Drivers, impacts and implications for subsurface ecosystems in urban areas. J. Contam. Hydrol. 248, 104021.

Becker, D., Epting, J., 2021. Thermal impact of subsurface urban structures on groundwater temperatures in the city of Basel. Grundwasser 26, 269–288.

Bidarmaghz, A., Choudhary, R., Soga, K., Kessler, H., Terrington, R.L., Thorpe, S., 2019. Influence of geology and hydrogeology on heat rejection from residential basements in urban areas. Tunn. Undergr. Space Technol. 92, 103068.

Bidarmaghz, A., Choudhary, R., Soga, K., Terrington, R.L., Kessler, H., Thorpe, S., 2020. Large-scale urban underground hydro-thermal modelling – A case study of the Royal Borough of Kensington and Chelsea, London. Sci. Total Environ. 700.

Bidarmaghz, A., Choudhary, R., Narsilio, G., Soga, K., 2021. Impacts of underground climate change on urban geothermal potential: Lessons learnt from a case study in London. Sci. Total Environ. 778.

Bloomer, J.R., 1981. Thermal conductivities of mudrocks in the United Kingdom. Q. J. Eng. Geol. 14, 357–362.

Blum, P., Menberg, K., Koch, F., Benz, S.A., Tissen, C., Hemmerle, H., Bayer, P., 2021. Is thermal use of groundwater a pollution? J. Contam. Hydrol. 239, 103791.

Breiman, L., Friedman, J., Olshen, R., Stone, C., 1984. Classification And Regression Trees, first ed. Routledge.

Brielmann, H., Lueders, T., Schreglmann, K., Ferraro, F., Avramov, M., Hammerl, V., Blum, P., Bayer, P., Griebler, C., 2011. Oberflächennahe Geothermie und ihre potenziellen Auswirkungen auf Grundwasserökosysteme. Grundwasser 16, 77–91.

Busby, J., Kingdon, A., Williams, J., 2011. The measured shallow temperature field in Britain. Q. J. Eng. Geol. Hydrogeol. 44, 373–387.

Casasso, A., Sethi, R., 2016. G.POT: A quantitative method for the assessment and mapping of the shallow geothermal potential. Energy 106, 765–773.

Dalla Santa, G., Galgaro, A., Sassi, R., Cultrera, M., Scotton, P., Mueller, J., Bertermann, D., Mendrinos, D., Pasquali, R., Perego, R., Pera, S., Di Sipio, E., Cassiani, G., De Carli, M., Bernardi, A., 2020. An updated ground thermal properties database for GSHP applications. Geothermics 85, 101758.

Epting, J., Böttcher, F., Mueller, M.H., García-Gil, A., Zosseder, K., Huggenberger, P., 2020. City-scale solutions for the energy use of shallow urban subsurface resources – Bridging the gap between theoretical and technical potentials. Renew. Energy 147, 751–763.

ESSO, 2019. Southampton to London Pipeline Project, Volume 6, Environmental Statement (Volume D), Appendix 8.1: Groundwater Baseline, Technical Report, National Infrastructure Planning, UK.

Ferguson, G., Woodbury, A.D., 2004. Subsurface heat flow in an urban environment. J. Geophys. Res.: Solid Earth 109, 1–9.

García-Gil, A., Vázquez-Suñe, E., Alcaraz, M.M., Juan, A.S., Sánchez-Navarro, J.Á., Montlleó, M., Rodríguez, G., Lao, J., 2015. GIS-supported mapping of low-temperature geothermal potential taking groundwater flow into account. Renew. Energy 77, 268–278.

García-Gil, A., Goetzl, G., Kłonowski, M.R., Borovic, S., Boon, D.P., Abesser, C., Janza, M., Herms, I., Petitclerc, E., Erlström, M., Holecek, J., Hunter, T., Vandeweijer, V.P., Cernak, R., Mejías Moreno, M., Epting, J., 2020. Governance of shallow geothermal energy resources. Energy Policy 138.

Gawecka, K.A., Taborda, D.M., Potts, D.M., Cui, W., Zdravković, L., Haji Kasri, M.S., 2017. Numerical modelling of thermo-active piles in London clay. Proc. Inst. Civil Eng.: Geotech. Eng. 170, 201–219.

Gilbey, M., Duffy, S., Thompson, J., 2011. The potential for heat recovery from london underground stations and tunnels. In: Proceedings of the CIBSE Technical Symposium, Leicester, UK, pp. 6–7.

Hähnlein, S., Bayer, P., Ferguson, G., Blum, P., 2013. Sustainability and policy for the thermal use of shallow geothermal energy. Energy Policy 59, 914–925.

Hart, O.E., Halden, R.U., 2020. Modeling wastewater temperature and attenuation of sewage-borne biomarkers globally. Water Res. 172, 115473.

Hastie, T., Tibshirani, R., Friedman, J., 2009. Elements of Statistical Learning. Springer.

Hawley, C., Fenner, R., 2012. The potential for thermal energy recovery from wastewater treatment works in southern england. J. Water Clim. Change 3, 287–299.

Highways Agency, 2015. M4 junctions 3 to 12 smart motorway, Development consent order application, Volume 6 – Environmental statement and related documents, Technical Report, Department for Transport, UK.

Jacob, K., Rosenzweig, C., Horton, R., Major, D., Gornitz, V., 2008. MTA Adaptations to Climate Change: A Categorical Imperative. Technical Report, Metropolitan Transportation Authority.

Jang, J., Narsilio, G.A., Santamarina, J.C., 2011. Hydraulic conductivity in spatially varying media—a pore-scale investigation. Geophys. J. Int. 184, 1167–1179.

Jones, L., Hulbert, A., 2017. User guide for the shrink-swell 3d (geosure extra) dataset v1.0. This item has been internally reviewed, but not externally peer-reviewed.

Koch, F., Menberg, K., Schweikert, S., Spengler, C., Hahn, H.J., Blum, P., 2021. Groundwater fauna in an urban area - Natural or affected? Hydrol. Earth Syst. Sci. 25, 3053–3070.

Lokoshchenko, M.A., Korneva, I.A., 2015. Underground urban heat island below Moscow city. Urban Clim. 13, 1–13.

Low, J.E., Loveridge, F.A., Powrie, W., 2017. Error analysis of the thermal cell for soil thermal conductivity measurement. Proc. Inst. Civil Eng. - Geotech. Eng. 170, 191–200.

Makasis, N., Kreitmair, M., Bidarmaghz, A., Farr, G., Scheidegger, J., Choudhary, R., 2021. Impact of simplifications on numerical modelling of the shallow subsurface at city-scale and implications for shallow geothermal potential. Sci. Total Environ. 791, 148236.

McDonnell Cole, 2020. Hydrogeological Risk Assessment for Central Park, Dagenham, Technical Report, Environment Agency, UK.

Menberg, K., Blum, P., Schaffitel, A., Bayer, P., 2013a. Long-term evolution of anthropogenic heat fluxes into a subsurface urban heat island. Environ. Sci. Technol. 47, 9747–9755.

Menberg, K., Bayer, P., Zosseder, K., Rumohr, S., Blum, P., 2013b. Subsurface urban heat islands in German cities. Sci. Total Environ. 442, 123–133.

Miocic, J.M., Krecher, M., 2022. Estimation of shallow geothermal potential to meet building heating demand on a regional scale. Renew. Energy 185, 629–640.

Müller, N., Kuttler, W., Barlag, A.B., 2014. Analysis of the subsurface urban heat island in Oberhausen, Germany. Clim. Res. 58, 247–256.

NCAS British Atmospheric Data Centre, 2020. Met office integrated data archive system (midas) land and marine surface stations data (1853-current).

Noethen, M., Hemmerle, H., Bayer, P., 2023. Sources, intensities, and implications of subsurface warming in times of climate change. Crit. Rev. Environ. Sci. Technol. 53, 700–722.

Ondreka, J., Rüsgen, M.I., Stober, I., Czurda, K., 2007. GIS-supported mapping of shallow geothermal potential of representative areas in south-western Germany-Possibilities and limitations. Renew. Energy 32, 2186–2200.

OpenStreetMap contributors, 2017. Data mining using the Overpass API in QGIS,https://www.openstreetmap.org.

Popiel, C.O., Wojtkowiak, J., 2013. Temperature distributions of ground in the urban region of Poznan City. Exp. Thermal Fluid Sci. 51, 135–148.

Previati, A., Epting, J., Crosta, G.B., 2022. The subsurface urban heat island in Milan (Italy) - A modeling approach covering present and future thermal effects on groundwater regimes. Sci. Total Environ. 810, 152119.

Price, S.J., Terrington, R.L., Busby, J., Bricker, S., Berry, T., 2018. 3D ground-use optimisation for sustainable urban development planning: A case-study from Earls Court, London, UK. Tunn. Undergr. Space Technol. 81, 144–164.

Ramos-Escudero, A., García-Cascales, M.S., Cuevas, J.M., Sanner, B., Urchueguía, J.F., 2021. Spatial analysis of indicators affecting the exploitation of shallow geothermal energy at European scale. Renew. Energy 167, 266–281.

RBKC, 2021. Planning and building control.

Rollin, K., 1987. G.R.P.B.G. Survey), Investigation of the Geothermal Potential of the UK: Catalogue of Geothermal Data for the Land Area of the United Kingdom; Third Revision; April 1987, British Geological Survey Geothermal Resources Programme.

Roshankhah, S., Garcia, A.V., Santamarina, J.C., 2021. Thermal conductivity of sand–silt mixtures. J. Geotech. Geoenviron. Eng. 147, 06020031.

Rotta Loria, A.F., Thota, A., Thomas, A.M., Friedle, N., Lautenberg, J.M., Song, E.C., 2022. Subsurface heat island across the Chicago Loop district: Analysis of localized drivers. Urban Clim. 44, 101211.

Santa, G.D., Peron, F., Galgaro, A., Cultrera, M., Bertermann, D., Mueller, J., Bernardi, A., 2017. Laboratory measurements of gravel thermal conductivity: An update methodological approach. Energy Proc. 125, 671–677.

Schiel, K., Baume, O., Caruso, G., Leopold, U., 2016. GIS-based modelling of shallow geothermal energy potential for CO2 emission mitigation in urban areas. Renew. Energy 86, 1023–1036.

Stephen, P., 2016. Cooling the Tube,https://www.railmagazine.com/infrastructure/stations/cooling-the-tube. Last accessed 25 August 2022.

Tissen, C., Benz, S.A., Menberg, K., Bayer, P., Blum, P., 2019. Groundwater temperature anomalies in central Europe. Environ. Res. Lett. 14.

Tissen, C., Menberg, K., Benz, S.A., Bayer, P., Steiner, C., Götzl, G., Blum, P., 2021. Identifying key locations for shallow geothermal use in Vienna. Renew. Energy 167, 1–19.

VDI, 2001. Blatt 2: Thermische Nutzung des Untergrundes–Erdgekoppelte Wärmepumpenanlagen (Part 2: Thermal use of the underground—ground source heat pump systems), VDI-4640/2, Technical Report. Verein Deutscher Ingenieure, Düsseldorf.

Walch, A., Li, X., Chambers, J., Mohajeri, N., Yilmaz, S., Patel, M., Scartezzini, J.-L., 2022. Shallow geothermal energy potential for heating and cooling of buildings with regeneration under climate change scenarios. Energy 244, 123086.

Waterman Infrastructure & Environment Limited, 2019. Detailed Derivation of Soil Parameters (Outstanding Issue 6) 68-86 Farringdon Road, Technical Report, Islington Council, UK.

WhatDoTheyKnow, 2011. Depth of tube lines. https://www.whatdotheyknow.com/request/depth_of_tube_lines. Accessed: 2021-08-23.